Journal of Marine Systems 204 (2020) 103286

Contents lists available at ScienceDirect

Journal of Marine Systems

journal homepage: www.elsevier.com/locate/jmarsys

Predicting the submesoscale circulation inshore of the East Australian Current

Colette Kerry[a,*], Moninya Roughan[a], Brian Powell[b]

[a] School of Mathematics and Statistics, Faculty of Science, UNSW Australia, Sydney, NSW, Australia
[b] Department of Oceanography, School of Earth and Ocean Sciences and Technology, University of Hawaii at Manoa, Hawaii, USA

ARTICLE INFO

Keywords:
Submesoscale
Shelf circulation
Western Boundary Currents
Cyclonic eddies
ROMS 4DVar

ABSTRACT

Submesoscale flows dominate the vertical transport in the upper ocean and play an important role in air-sea fluxes, the distribution of nutrients and biota, the connectivity of populations. Yet submesoscale predictability is a new frontier and presents additional challenges to that of mesoscale flows. This study assesses the capacity of an operational system to predict the circulation along the landward edge of the East Australian Current where the cyclonic band of vorticity allows small scale instabilities to grow. We use a downscaling approach in which a fine-scale resolution (750–1000 m) coastal model is one-way nested within a coarser resolution (2.5–6 km) mesoscale eddy-resolving regional model that assimilates all available data, including coastal high-frequency radar radial velocities. Assimilation of the surface radial velocities into the regional model provides improved representation of the cyclonic band inshore of the current, however forecasts at this resolution perform poorly in representing this cyclonic vorticity. Downscaling to the higher resolution coastal model produces a sharper across-current vorticity gradient within the EAC and leads in turn to more intense submesoscale features growing on its inshore side. Boundary forcing error from the regional model propagates into the nested coastal model. The results motivate improved representation of fine-scale flows in regional forecasts for downscaling purposes.

1. Introduction

The circulation on continental shelves influenced by Western Boundary Currents (WBC) is typically characterised by complex shelf dynamics including high cross-shelf variability. Submesoscale features (filaments and eddies) form on the edges of the WBC and have a profound impact on the shelf circulation (Gula et al., 2014; Schaeffer et al., 2017), impact the connectivity of populations (Bracco et al., 2016), and play important roles in the distribution of nutrients and biota (Everett et al., 2015; Mantovanelli et al., 2017; Roughan et al., 2017).

Submesoscale flows are defined dynamically as flows characterised by high Rossby number or low Richardson number (Hetland, 2017; Thomas et al., 2008). The Rossby number ($Ro = |\zeta/f|$) describes the ratio of local vorticity to planetary rotation; for mesoscale flows (Ro≪1) planetary rotation dominates local vorticity, while submesoscale features are characterised by Rossby numbers of O(1). The gradient Richardson number describes the ratio between buoyancy and shear and is given by $Ri = N^2/|\partial_z \mathbf{u}_H|^2$, where $N^2 = \frac{-g}{\rho}\frac{\partial \rho}{\partial z}$ is the buoyancy frequency and $\mathbf{u}_H$ is the horizontal velocity (Thomas et al., 2008). Mesoscale flows are buoyancy driven (Ri $>>$ 1) while submesoscale flows can be characterised by Richardson numbers of O(1).

Operational ocean forecasts available at present, with model resolutions of about 10 km(e.g. Metzger et al., 2014), typically resolve the mesoscale circulation with features of horizontal extent of O(100 km). Predictive skill of the slowly-evolving mesoscale flows (time scales of weeks to months) has continued to increase through improvements in modelling and data assimilation techniques that focus on reducing the error at the beginning of the forecast window. With increased computational resources and model efficiency, there is a move towards higher resolution ocean models that are capable of capturing more fine-scale features that are important in many coastal regions (e.g. submesoscale eddies, coastal upwelling, shelf fronts) with horizontal scales of 1–100 km. These fine-scale features are typically rapidly-evolving (time scales of hours to days), so the forecasts are more quickly decorrelated from the initial state with greater dependence on model configuration, parameters, boundary and surface forcings. As such, the prediction of fine-scale features presents additional challenges and may require a different approach to that of the mesoscale circulation (Duda et al, 2014).

The East Australian Current (EAC), the WBC of the South Pacific Subtropical Gyre, interacts with the continental shelf and typically separates from the coast between 31 and 33° S (Fig. 1, Cetina-Heredia

* Corresponding author.
E-mail address: c.kerry@unsw.edu.au (C. Kerry).

https://doi.org/10.1016/j.jmarsys.2019.103286
Received 16 January 2019; Received in revised form 4 October 2019; Accepted 3 December 2019
Available online 23 December 2019
0924-7963/

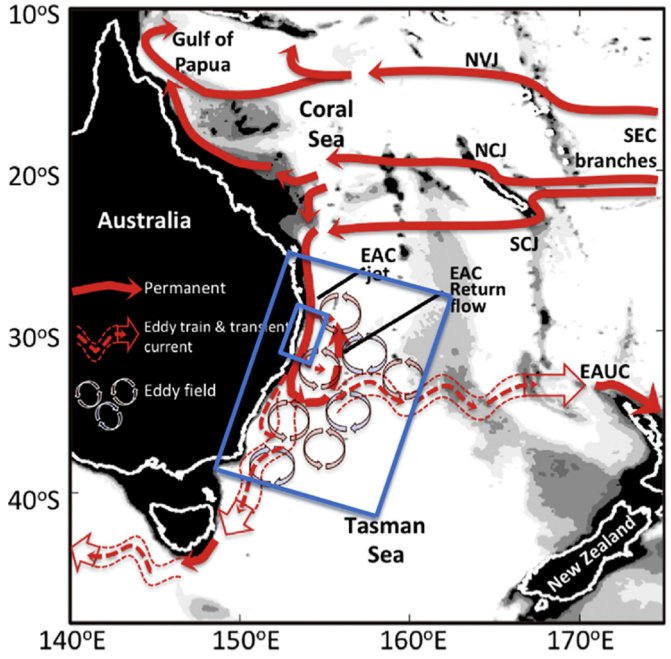

Fig. 1. Schematic of the Southwestern Pacific surface ocean circulation showing the EAC system, adapted from Oke et al. (2019). Regional (EAC) and Coastal (COFFS) model domains are shown by the blue lines.

et al., 2014; Oke et al., 2019). This separation results in episodic upwelling of slope water onto the shelf (Oke and Middleton, 2000; Roughan and Middleton, 2004) and the formation of an energetic mesoscale eddy field in the Tasman Sea (Fig. 2a, Wilkin and Zhang, 2007). Upstream of its separation, the current core is typically located over the continental shelf break (Kerry et al., 2018, their Fig. 1c and d). Submesoscale flows that form on the current's landward side consist of a mixture of fronts and eddies and Schaeffer et al. (2017) suggest that frontal eddies observed inshore of the EAC at 30°S are well described by the theory of baroclinic waves. Baroclinic instabilities in the mixed layer can develop around the larger, geostrophic, mesoscale eddies or along the edges of boundary currents and are also shown to generate submesoscale flows in the Gulf Stream Region (Callies et al., 2015), the Gulf of Mexico (Luo et al., 2016), and the Subtropical North Pacific (Qiu et al., 2014) for example.

Recent modelling work in the EAC has combined a state-of-the-art numerical ocean model with a variety of traditional and newly available observations to generate an ocean state estimate of the EAC region at 2.5–6 km resolution (Kerry et al., 2016). Using the reanalysis, Kerry et al. (2018) show that observations taken in regions with greater oceanic variability contribute the most to modelled estimates of EAC transport and mesoscale eddy variability. While the above studies focus on state estimation, forecast skill of this EAC model is presented in Roughan et al. (2018) which shows that the system is effective for mesoscale circulation forecasts but suggests further tuning and/or downscaling to provide accurate predictions close to the coast, on the shelf and shelf slope. Prior to these studies, prediction studies in the EAC had been at resolutions insufficient to resolve the continental shelf or circulation features of spatial scales smaller than the mesoscale (e.g. Oke et al., 2013, 2008 at 10 km resolution and Zavala-Garay et al., 2012 at 18–30 km resolution).

This study shows the capacity of an operational system to reproduce inshore coastal submesoscale features by downscaling a regional mesoscale eddy-resolving model that is data-constrained. Using the 2-year reanalysis of the EAC system for the years 2012–2013 covering southeastern Australia (Kerry et al., 2016), we have downscaled to a model that partially resolves the submesoscale dynamics around Coffs Harbour (29–31.5°S, 750–1000 m model resolution) to study the predictability of fine-scale flows. We focus on the prediction of the circulation along the landward edge of the EAC where the cyclonic band of vorticity allows small scale instabilities to grow.

The Coffs Harbour region (30°S) provides an ideal study site to investigate the predictability of the coastal circulation as it exhibits complex shelf dynamics. Submesoscale eddies occur irregularly inshore of the EAC here, on average every 7 days, with typical inshore radii of ~10 km (Schaeffer et al., 2017). In addition, the Coffs Harbour region is well observed having been instrumented through the Australian Integrated Marine Observing System program since 2010 (IMOS; http://imos.org.au). Sustained observations include surface current velocities at 1.5 km spatial resolution up to 150 km offshore from a high-frequency (HF) radar array, sub-surface observations of temperature and velocity from two coastal moorings, and repeat hydrographic transects from autonomous ocean gliders over the past 10 years (Roughan et al., 2010, 2015). The surface current velocity measurements from the HF radar array provide an invaluable tool for the identification of submesoscale features (that are too small to be resolved by altimetry).

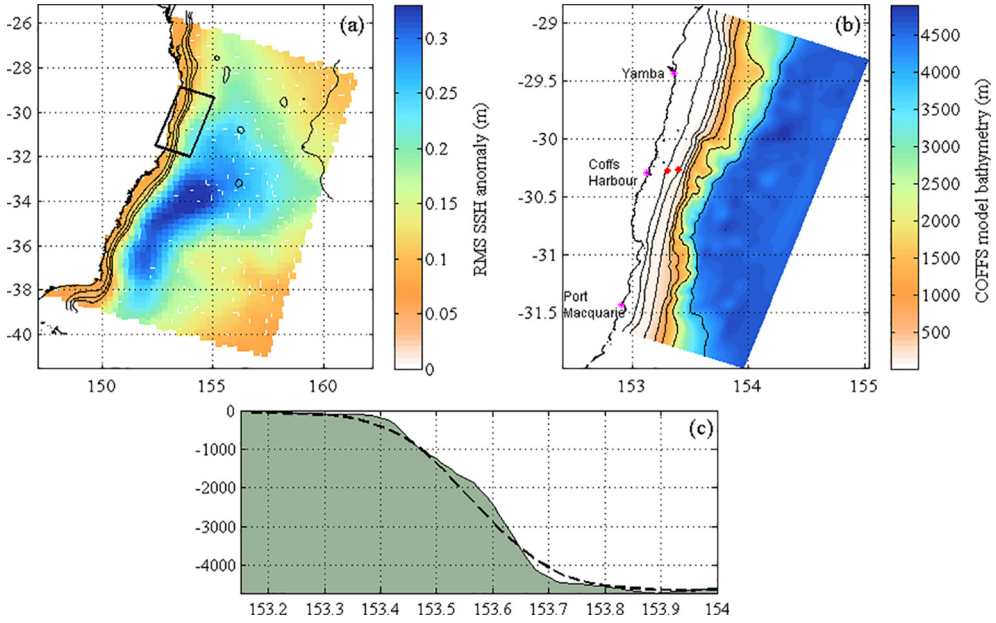

Fig. 2. Root-Mean-Squared SSH anomaly for 20 years of AVISO observations over the EAC domain, showing 200, 1000 and 2000 m EAC model bathymetry contours (black lines) and the COFFS domain, (a). COFFS model bathymetry with 70, 100, 200, 500, 1000, 2000 and 4000 m contours, towns marked by magenta stars and Coffs Harbour shelf moorings (CH070 and CH100) shown by red diamonds, (b). Comparison of COFFS model bathymetry (green fill) and EAC model bathymetry (black dashed line) for a cross-shore section crossing the coast at Coffs Harbour (30.3°S).

In Section 2 we describe the modelling system, which encompasses a data-assimilating regional model of the EAC system and a nested higher resolution model around Coffs Harbour. Section 3 presents the results in terms of predictive skill; firstly we quantify the predictive skill with respect to available observations across the nested model domain, then we focus on the representation of vorticity and frontal eddies inshore of the EAC. The implications of the results in terms of fine-scale predictability are discussed in Section 4 and recommendations for future study are made. The work is summarised and conclusions are drawn in Section 5.

2. Modelling system

2.1. The regional(EAC) model

The regional model (hereafter called the EAC model) is presented in Kerry et al. (2016). The model domain extends from Fraser Island in the north (25.25 °S) to south of the New South Wales/Victoria border (41.55 °S) and approximately 1000 km offshore. The domain encompasses the EAC system from where it is most coherent (Sloyan et al., 2016) to where it separates from the coast and forms an energetic eddy field in the Tasman Sea (refer to Fig. 1). The model has a 2.5 –6 km cross-shore resolution and a 5 km alongshore resolution, with 30 vertical s-levels distributed with a higher resolution in the upper 500 m to resolve the wind-driven mesoscale circulation and near the bottom to resolve the bottom boundary layer. Boundary forcing is provided by the BlueLink Reanalysis (BRAN3p5, Oke et al., 2013) and atmospheric forcing by the 12 km resolution Bureau of Meteorology (BOM) Australian Community Climate and Earth-System Simulation (ACCESS) analysis (Puri et al., 2013).

A variety of ocean observations are assimilated into the EAC model, using strong-constraint incremental 4-Dimensional Variational Data Assimilation (4D-Var), to generate a 'best estimate' of the ocean state over a 2-year period (January 2012–December 2013). This data assimilation method uses the model dynamics to perturb the initial conditions, atmospheric forcing, and boundary conditions (the control vector) such that the modelled ocean state better fits and is in balance with the observations (Di Lorenzo et al., 2007; Moore et al., 2011). The assimilation configuration, the observations, and the processing of observations prior to assimilation are described in detail in Kerry et al. (2016).

The observations include satellite-derived gridded Sea Surface Height (SSH) fields from AVISO (1/4° × 1/4 °, CNES, 2015), satellite-derived Sea Surface Temperature (SST) from the US Naval Oceanographic Office Global Area Coverage Advanced Very High Resolution Radiometer level-2 product (4 km resolution, Andreu-Burillo et al., 2010), temperature and salinity from Argo profiling floats (www.argo.ucsd.edu), temperature profiles from expendable bathythermograph (XBT) lines, along with newly available observations that were collected as part of Australia's IMOS. These include full-water-column velocity and hydrographic observations from a deep-water mooring array extending offshore from Brisbane (27.5 °S, Sloyan et al., 2016) and several moorings on the continental shelf (Roughan et al., 2015), temperature and salinity observations from ocean gliders (Roughan et al., 2018) and HF radar observations of surface radial currents at Coffs Harbour (30 °S, Wyatt, 2015; Wyatt et al., 2018).

The locations and types of all of the assimilated observations with the exception of the Argo floats and the satellite-derived surface observations are shown in Fig. 3a. The Argo floats that are assimilated over the 2-year period provide coverage across the entire domain (refer to Fig. 5a in Kerry et al., 2016). Fig. 3b and c show the percent coverage of the surface radial velocity observations over the 2-year period for the two HF radar sites (named NNB and RRK). The radars provide surface radial velocity measurements every 10 min at 1.5 km spatial resolution out to a maximum of 150 km offshore. The radial velocities are gridded on to the model grid and daily-averaged for assimilation into the EAC model. While surface velocities can only be computed where the measured radial coverage overlaps, we assimilate the radial velocities directly (De Souza et al., 2015) allowing us to make use of the maximum amount of data. The validation provided by Kerry et al. (2016) showed that, upon data assimilation, the ocean state estimates represent both assimilated and non-assimilated observations well.

2.2. The coastal(COFFS) model

The coastal model is centred around Coffs Harbour (hereafter called the COFFS model, Fig. 2b) and encompasses the region of coverage of the HF radar observations (Fig. 3b and c). This region is dynamically interesting and an ideal location to study shelf circulation impacted by the EAC. Situated just upstream of the area of elevated SSH variability, indicative of enhanced eddy activity formed as the EAC separates from the coast (Fig. 2a), the COFFS model domain covers a section of the shelf where the EAC separates often (Cetina-Heredia et al., 2014) and frontal eddies form along the inshore edge of the EAC on average every 7 days (Schaeffer et al., 2017).

The COFFS model has a varying horizontal resolution in the cross-shore direction of 750–1000 m, with the 750 m resolution covering the entire shelf and shelf slope and increasing gradually offshore. The alongshore resolution is 900 m. The model has 30 terrain following s-levels distributed with a higher resolution in the upper 500 m and near the bottom, using the stretching scheme described in De Souza et al. (2015). The bathymetry for the model was obtained from the 50 m Multibeam Dataset for Australia from Geoscience Australia (Whiteway, 2009) and some topographic smoothing was applied to minimise horizontal pressure gradient errors to an acceptable level (Haney, 1991; Mellor et al., 1994). The model resolution allows for a considerably better representation of the continental shelf and slope bathymetry than the EAC model (Fig. 2c), with a wider continental shelf and a sharper shelf break in the COFFS model. At the boundaries, the COFFS model bathymetry is merged with the EAC model bathymetry to ensure a seamless transition of the nested flows. In particular, the northern boundary required careful merging as the EAC bathymetry has a narrower shelf and a less steep continental shelf due to the required topographic smoothing.

The COFFS model is one-way nested inside the EAC model (described above) with the boundary forcing applied 4-hourly. The Chapman condition (Chapman, 1985) is applied to the free surface and the Flather condition (Flather, 1976) is applied to the barotropic velocity so that barotropic energy is effectively transmitted out of the domain. Radiation conditions are applied at the boundaries and baroclinic energy that does not match the incoming boundary condition is absorbed using a flow relaxation scheme involving a sponge layer. The width of the sponge layer, over which viscosity and diffusivity are increased linearly by a factor of 10 from the values applied within the model domain, is 30 grid cells wide at the northern boundary and 10 grid cells at the eastern and southern boundaries.

We use atmospheric forcing from the Bureau of Meteorology Atmospheric high-resolution Regional Reanalysis for Australia (BARRA), downscaled to 1.5 km resolution over the southeastern Australia coastal region (BARRA-SY, http://www.bom.gov.au/research/projects/reanalysis/, Jakob et al., 2017). The atmospheric forcing fields are specified hourly and used to compute the surface wind stress and surface net heat and freshwater fluxes using the bulk flux parameterisation of Fairall et al. (1996). The longwave radiation in the atmospheric boundary layer is computed internally using the Berliand and Berliand (1952) equation as a function of air temperature, sea surface temperature, relative humidity and cloud fraction. Tidal forcing is applied at the boundaries with tidal surface elevation and momentum from the global barotropic tidal model provided by the Oregon State University TOPEX/Poseidon Global Inverse Solution, TPXO8, (Egbert and Erofeeva, 2002). Tidal elevations from the COFFS model compare well to tide gauge data at Yamba, Coffs Harbour and Port Macquarie

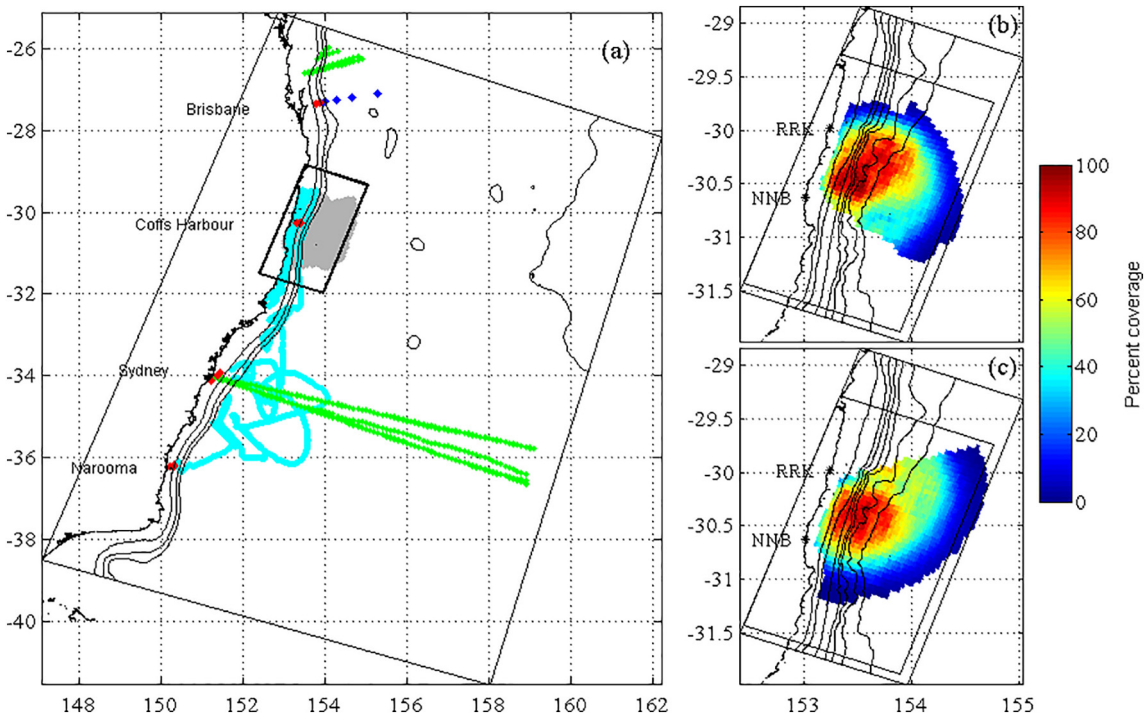

Fig. 3. Observations assimilated into the EAC reanalysis (excluding Argo and satellite observations, not shown), (a). XBT (green), Glider (cyan), shelf moorings (red), EAC array (blue) and HF radar (grey). The 200, 1000 and 2000 m EAC model bathymetry contours are shown (black lines). Percent coverage of HF radar surface radial current observations over the 2-year (2012–2013) time period for site NNB (b) and site RRK (c).

(see locations on Fig. 2b) obtained from Manly Hydraulics Laboratory (https://mhl.nsw.gov.au/data, not shown).

2.3. Prediction system

The prediction system encompasses the high-resolution COFFS model one-way nested inside the EAC model. The modelling methodology over the 2-year (2012–2013) test period is outlined in the flow chart in Fig. 4. The EAC model forecast and analysis sequences are performed over subsequent 5-day windows which are overlapped by 1-day, such that every four days a new forecast and analysis is performed. Because the linearised model equations are used for the 4D-Var minimisation procedure, the length of the assimilation window is limited by the time over which the tangent linear assumption remains reasonable (in this case 5 days, Kerry et al., 2016). For the very first EAC forecast, the initial conditions are taken from BRAN3p5, and for all subsequent forecasts the initial state is provided by the previous analysis, as per the flow chart in Fig. 4. The EAC forecast model state is combined with observations over the 5-day window using 4D-Var data assimilation, which solves for increments in model initial conditions, boundary conditions and surface forcing such that the difference between the new modelled solution and all available observations is minimised – in a least-squares sense – over the assimilation window. Applying these increments and integrating the nonlinear ocean model over the 5 days provides the 'best estimate' of the ocean state (the EAC analysis) which is constrained to satisfy the nonlinear model equations (strong-constraint) and better represent the observations over the assimilation window. The analysis provides an improved estimate of the initial state for the subsequent EAC forecast, and the procedure is repeated. The EAC model outputs are saved 4-hourly.

Nested inside the EAC forecasts and analyses described above are the COFFS forecasts and hindcasts, respectively. The COFFS forecast is a 5-day simulation that is one-way nested within the EAC forecast. It takes its initial conditions and boundary forcing from the EAC forecast, but is provided with higher resolution atmospheric forcing (BARRA-SY) and includes tides (TPXO). Likewise, the COFFS hindcast is a 5-day free-running simulation that takes its initial conditions and boundary forcing from the EAC analysis. For the COFFS model, the model outputs are saved 2-hourly.

3. Results

3.1. Assessment of predictive skill

We begin by assessing the predictive skill of the EAC forecasts and analyses and the COFFS forecasts and hindcasts with respect to available observations over the 5-day windows. To facilitate these comparisons, we output the model values at the times and locations corresponding to the observations. For SST we compute the Root-Mean-Squared (RMS) error between the observations and the model, output at the observation times and locations, for all observations across the domain (for the EAC model we use only observations within the COFFS model domain). The SST observations used are the same observations that are assimilated into the EAC model (daily at 4 km spatial resolution in the absense of clouds), and the RMS error is computed for 12-hour time periods over the 5 days to show how the predictive skill changes over the length of the window (Fig. 5a). The RMS SST error is around 0.4°C over the entire EAC analysis window, while in the COFFS hindcast the error increases from 0.4°C over the first day to 0.5°C by the fifth day. The EAC forecast and COFFS forecast errors are of the same magnitude, increasing from 0.4°C in the initial conditions to 0.6°C at the end of the 5-day forecast window. There is an improvement on persistence (that assumes the SST does not evolve over the 5 days) that gives an error of 0.7°C by days 3–5.

Velocities are measured by acoustic Doppler current profilers (ADCPs) located on two shelf moorings off Coffs Harbour, CH100 and CH070 (located in 100 m and 70 m water depths respectively, locations shown by red diamonds in Fig. 2b). Only mooring observations from CH100 were assimilated into the EAC model as the model poorly resolves the shelf at CH070 (there are only 3 grid cells between the

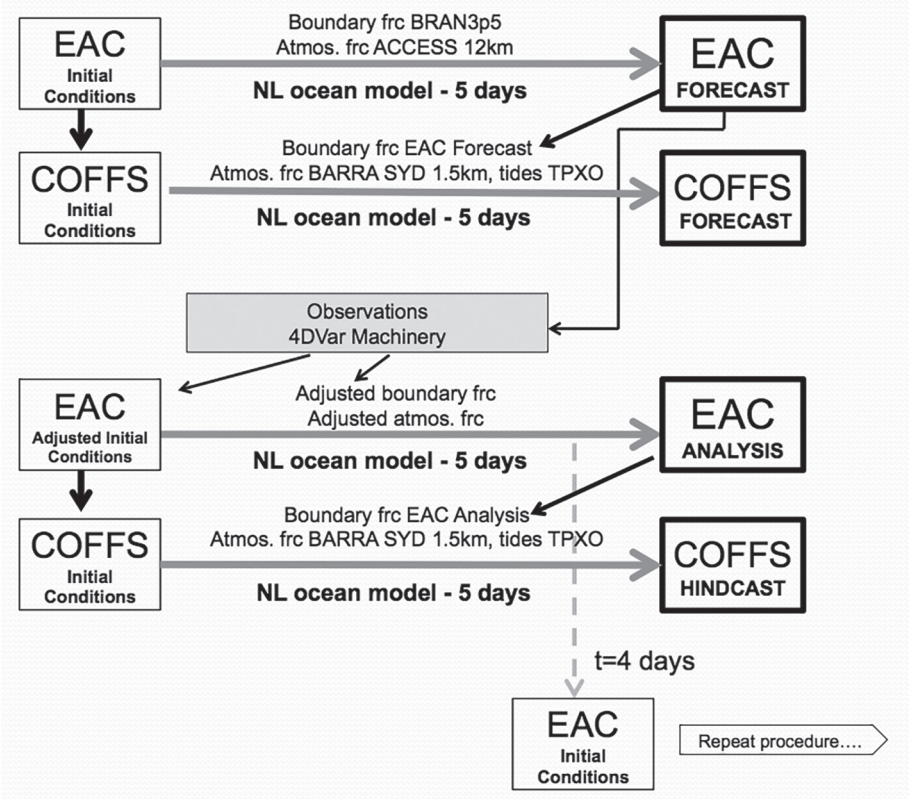

Fig. 4. Flow chart showing the prediction system. NL = nonlinear, frc = forcing.

locations of CH070 and CH100 in the EAC model). Velocity measurements were low-pass filtered at 30 h to remove tidal and inertial oscillation variability, and applied 6-hourly for assimilation into the EAC model. Profiles in Fig. 5b for the EAC analysis and the EAC forecast show the complex correlation of these processed velocity observations compared to the corresponding model values with depth. For the analysis the complex correlations range from 0.95 in the upper 30 m to 0.83 at the deepest measurement (90 m depth).

For comparison with the COFFS models, hourly-averaged velocity observations are generated from the raw velocity observations, such that they still include the tidal flows but exclude the very high frequency, small-scale flows that are not resolved by the model. The representation of the continental shelf is considerably better in the COFFS model, with CH070 and CH100 being located in the correct water depths and 11 grid cells separating the moorings. The complex correlations of these velocities with the corresponding values from the COFFS hindcasts range from 0.92 near the surface to 0.75 at the bottom, consistently about 0.03 less than the EAC analysis throughout the water column. Although the comparisons are being made against higher temporal resolution velocities for the COFFS forecasts, compared to the parent EAC forecasts, the complex correlations remain the same throughout the water column at CH100, ranging from 0.89 near the surface to about 0.75 at depth. At CH070 (Fig. 5c), the COFFS modelled and observed velocities are slightly less well correlated than at CH100, with the hindcast correlations ranging from 0.86 to 0.75 and the forecast correlations from 0.83 to 0.71, where the lower correlations are at the base of the water column.

High frequency temperature measurements are also made at CH100 and CH070, and they are processed in the same way as the velocity observations for assimilation into the EAC model and for comparison with the EAC and COFFS models (the EAC observations are low-pass filtered at 30 h and applied 6-hourly, and the COFFS observations are hourly). Anomaly Correlation Coefficient (ACC) profiles and RMS error profiles for the temperature observations are shown in Fig. 5 d–e and f–g, respectively. For the ACC, the anomalies in each depth bin are computed with respect to the time mean of all values in that particular depth bin. The ACC describes how well correlated the time series are, while the RMS error quantifies the magnitude of the errors. At CH100 the COFFS hindcast, EAC forecast and COFFS forecast all have similar magnitudes for both metrics in the upper 30 m, below which the forecasts degrade slightly compared to the hindcast. The temperature ACCs are similar at CH070 as at CH100 for the COFFS hindcasts and forecasts while the RMS temperature errors are less at CH070.

Surface velocities can be computed where the measurements of the radial surface currents from the two HF radar sites overlap. For the EAC model, daily-averaged radial surface velocities were assimilated (described in Kerry et al., 2016), and Fig. 6 shows the complex correlations of surface velocities computed from the assimilated values and the corresponding model values for the EAC analyses (row a) and the EAC forecasts (row b). The black lines show the 0.9 complex correlation contour. Note that for the EAC analyses the correlation is greater than 0.9 across all 5 days. Values inside the 50 m raw bathymetry contour are not plotted as the velocity values are considered unreliable here due to Geometric Dilution of Precision (Wyatt et al., 2018). Note that the radial velocities do not suffer from these errors and are assimilated inside of the 70 m contour into the EAC model, and the RMS errors between the analysis and observed radial velocity values show no degradation in skill inside of the 70 m contour (not shown).

The comparisons against the surface velocities from the COFFS model are made against surface velocities computed from the surface radial velocities processed as in Archer et al. (2017), where hourly radials are generated using a Hanning window. The complex correlations for the hourly surface velocities with the corresponding modelled values from the COFFS hindcasts and COFFS forecasts are shown in Fig. 6 (rows c and d, respectively). Complex correlations inshore of the 70 m model bathymetry contour are poor for all days of the COFFS hindcasts and forecasts as the velocities computed from the radial velocity measurements may be unreliable here due to Geometric Dilution

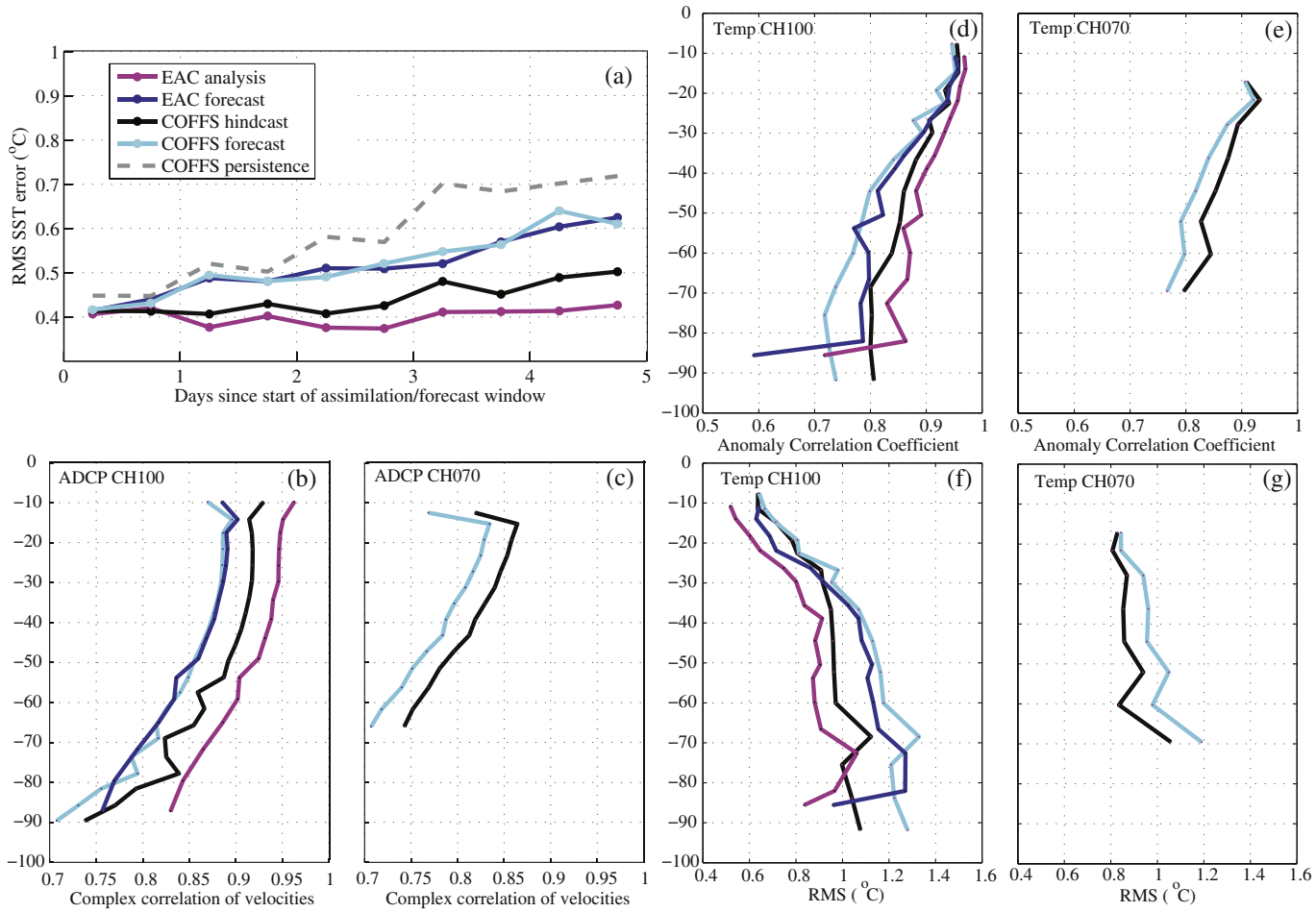

Fig. 5. Root-Mean-Squared SST error for days 0–5 of the assimilation/forecast windows, spatially-averaged over the COFFS model domain and averaged over all windows, (a). Complex correlation of velocities measured by ADCPs at CH100 (b) and CH070 (c). Anomaly Correlation Coefficient of temperature measured at CH100 (d) and CH070 (e). Root-Mean-Squared error of temperature measured at CH100 (f) and CH070 (g).

of Precision (Wyatt et al., 2018) or the model may not adequately resolve the complex shelf circulation.

3.2. 4D-Var increment adjustments

The EAC analysis employs incremental 4D-Var which adjusts the initial and boundary conditions and the surface forcing such that the difference between the model solution and the observations is minimised, in a least squares sense, over the assimilation time window. The magnitude and spatial distribution of the adjustments are dependent on the observations, the model-observation differences and the prior specification of the observation and model background errors. As described in Kerry et al. (2016), the prior background and observation uncertainties were carefully chosen and are shown to be reasonable allowing the analysis to achieve reduced uncertainty with a reasonable level of optimality (refer to Section 4.1 of Kerry et al., 2016). Given the consistency of the assimilation system, the increment adjustments made during the assimilation can provide insight into potential sources of model error.

To understand the relative magnitudes of the increment adjustments, we normalise the adjustments by an estimate of the typical variability of the corresponding state variable or forcing field value over a 5-day period (the length of the assimilation window). For the normalisation we use standard deviations that were estimated from the average of 5-day variances from the 10-year free running model described in Kerry et al. (2016). These are the same standard deviations used to estimate the background error covariances for the assimilation.

In Fig. 7, the mean of the absolute value of the normalised increment adjustments to the initial conditions and surface forcing for each 5-day assimilation window are plotted as time series (boundary forcing increments are not shown). For the initial conditions the values are the spatial average (over the entire EAC model domain, Fig. 7a, and over the COFFS domain region, Fig. 7b) of the absolute value of the normalised increments at $t = 0$. For the boundary and surface forcing we take the mean magnitude of the adjustments made over the 5-day window (the boundaries are updated daily and the forcing 12-hourly). The normalised surface forcing increments are spatially averaged over the entire EAC model domain (Fig. 7c) and over the COFFS domain region only (Fig. 7d).

The greatest adjustments in the initial conditions are made to SSH and temperature. The spatially averaged normalised increments (increment magnitudes) for initial conditions, averaged over the 2 years and over the entire EAC domain, are 89% (2.6 cm), 77% (0.18°C), 51% (0.038 ms^{-1}), 44% (0.0087) and 38% (0.027 ms^{-1}) for SSH, temperature, alongshore velocity, salinity, and cross shore velocity, respectively. The percentages are representative of the mean increment adjustment relative to the typical variability of the variable over a 5-day period and allow comparison of the relative adjustments of different variables. Over the COFFS domain region, the normalised initial condition adjustments are greater than the entire EAC domain averages for all variables except SSH. The normalised increments for initial conditions, averaged over the 2 years and over the COFFS domain, are 78%, 89%, 102%, 86% and 57% for SSH, temperature, alongshore velocity, salinity, and cross shore velocity, respectively. On average, the

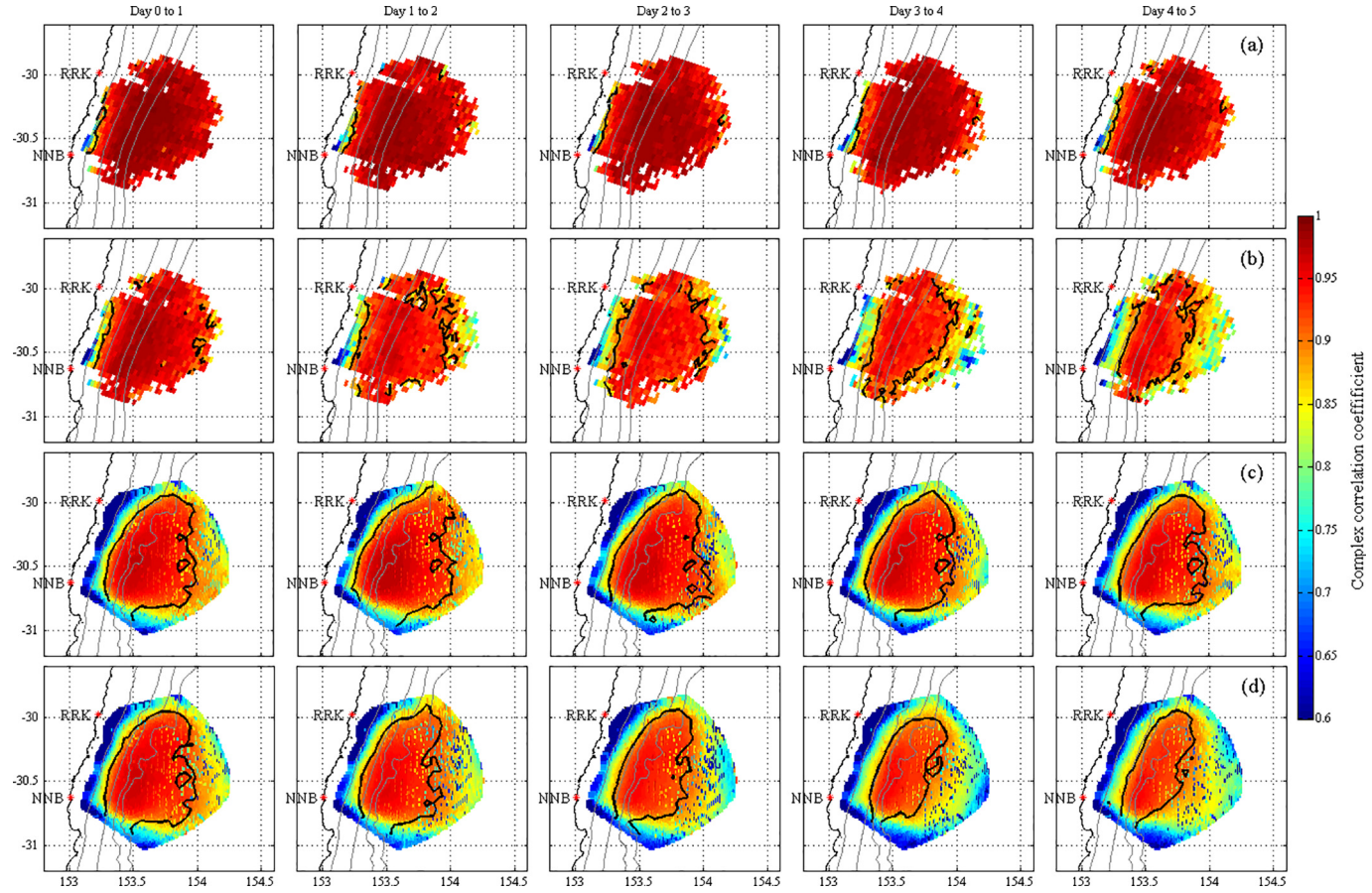

Fig. 6. Complex correlation of daily-averaged surface velocities measured by the HF radar with EAC analyses (row a) and EAC forecasts (row b), separated by window day. Complex correlation of hourly surface velocities measured by the HF radar with COFFS hindcasts (row c) and COFFS forecasts (row d), separated by window day. Black lines show to 0.9 complex correlation contour and grey lines show the 70, 200, 1000 and 2000 m model bathymetry contours. Only grid cells with a minimum of 15 velocity values over the 2-year period are shown, and values inside the 50 m bathymetry contour are removed as the computed velocities are unreliable here due to Geometric Dilution of Precision (Wyatt et al., 2018).

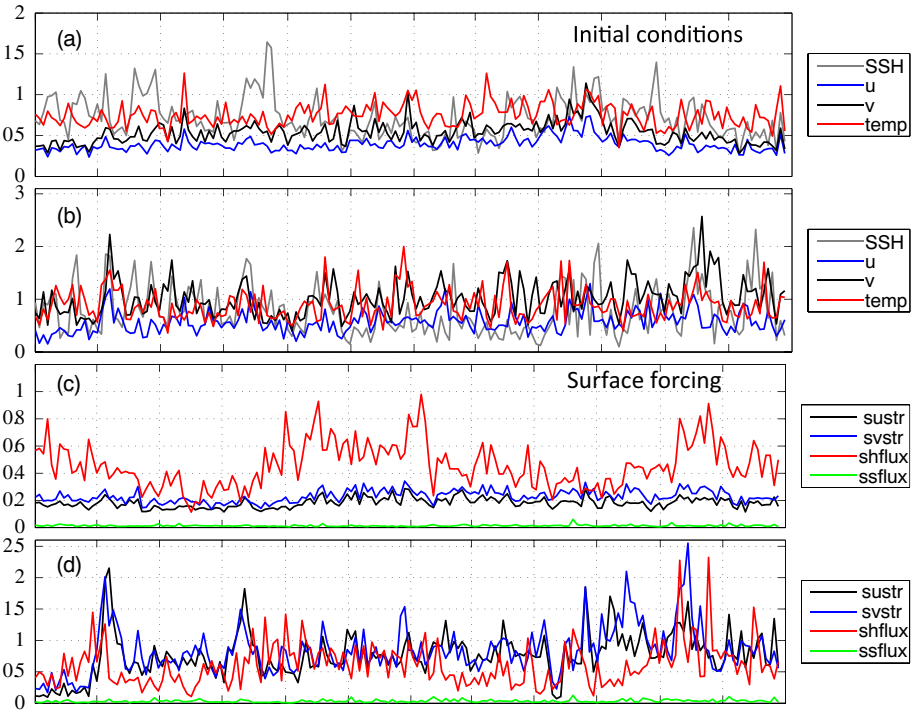

Fig. 7. Time series of increment adjustments, normalised by 5-day standard deviations, made to the initial conditions and surface forcing for the 2-year EAC analysis. The increment adjustments to the initial conditions spatially-averaged over the entire EAC domain (a), to the initial conditions spatially-averaged over the COFFS model domain (b), to the surface forcing spatially-averaged over the entire EAC domain (c) and to the surface forcing spatially-averaged over the COFFS model domain (d). (sustr = surface cross shore wind stress, svstr = surface alongshore wind stress, shflux = surface heat flux, ssflux = surface salinity flux.).

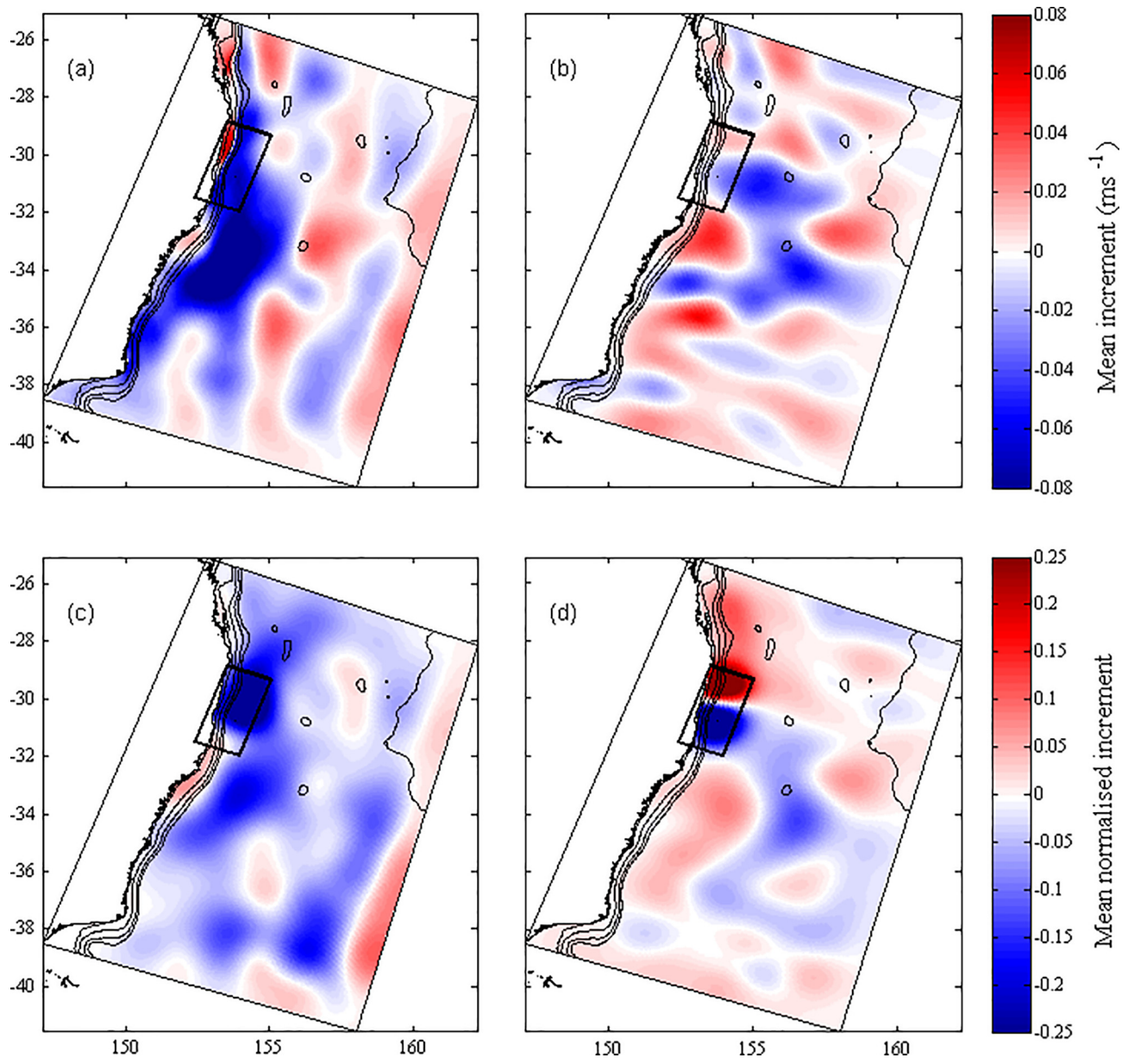

Fig. 8. Mean increment to initial conditions in the EAC analyses for surface alongshore velocity (a) and surface cross-shore velocity (b). Mean increments to the wind stress forcing for the EAC analyses (alongshore, (c), and cross-shore, (d)), normalised by 5-day standard deviations. The 70, 200, 1000 and 2000 m EAC model bathymetry contours are shown (black lines) as is the COFFS model domain. Note that the velocity increments are not normalised, as the velocity values in ms^{-1} are more intuitively interpreted, while the wind stress increments have been normalised.

alongshore velocity increments over the COFFS domain are of the same magnitude as the typical variability over the assimilation window period. Note that the salinity increments are not shown in Fig. 7a and b for clarity.

For surface forcing, averaged over the entire EAC domain, the greatest adjustment is made to the surface heat flux, with a normalised increment (increment magnitude) of 49% (52 Wm^{-2}) on average over the 2 years. Over the COFFS domain region, adjustments to the surface wind forcing is considerably greater, with normalised increment adjustments of 83% and 75% for alongshore and cross-shore wind stress on average over the 2 years (compared to 23% and 18% for the EAC domain averages).

At the EAC model boundaries (increment adjustments not shown in Fig. 7), temperature is adjusted most at the northern (upstream) boundary, compared to the southern and eastern boundaries, with a mean normalised increment (increment magnitude) of 26% (0.041°*C*) over the 2 years. Alongshore velocity is adjusted at the northern and southern boundaries with 2-year average normalised increments (increment magnitudes) of 41% (0.014 ms^{-1}) and 33% (0.012 ms^{-1}), respectively.

In order to better represent the circulation inshore of the EAC over the COFFS domain region, as observed by the HF radar array, the EAC model makes its greatest adjustments to the alongshore velocity initial conditions. The wind stress surface forcing is also adjusted considerably more over this region than over the rest of the domain. In the initial conditions, the mean velocity increments over the COFFS model domain region are such that there is increased equator-ward velocity on the shelf and increased poleward velocity offshore of the 1000 m contour, with an associated increase in onshore velocity in the southern region of the COFFS domain and an increase in offshore velocity to the north (Fig. 8a and b). While the initial condition adjustments can introduce or enhance the cyclonic features at the beginning of the

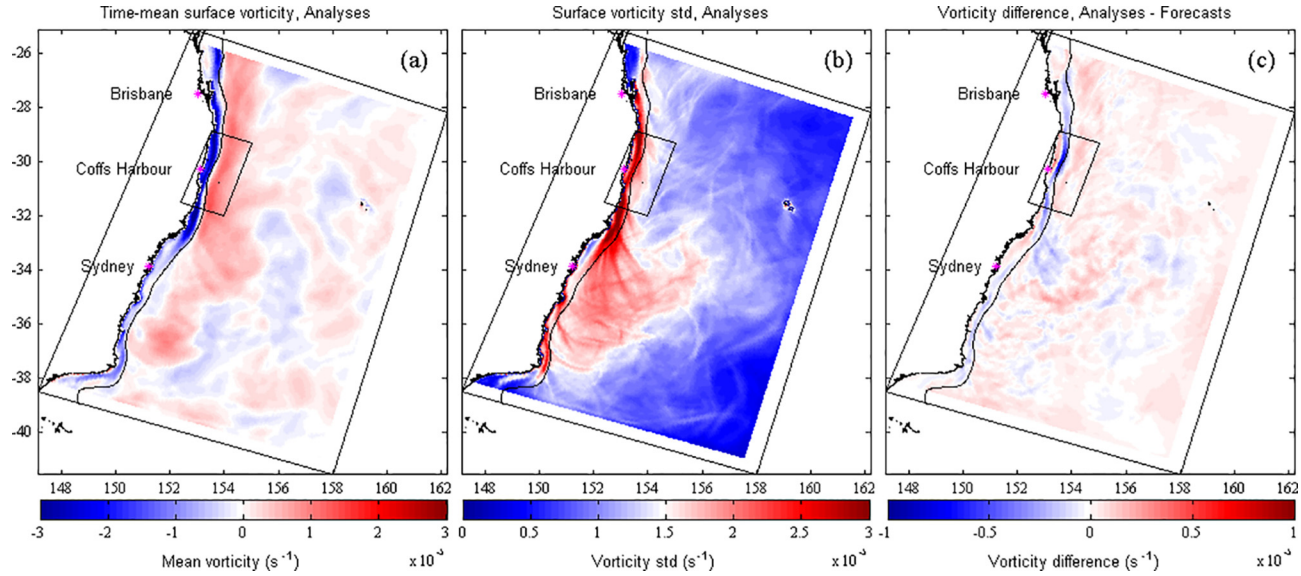

Fig. 9. Time-mean surface vorticity from the EAC analyses (a), standard deviation of surface vorticity computed from 4-hourly snapshots from the EAC analyses (b) and time-mean surface vorticity difference between the EAC analyses and forecasts (c). The 1000 m EAC model bathymetry contour and the boundaries of the COFFS domain are shown (black lines). The plots exclude 10 grid cells inside of the boundaries (the sponge layer). Vorticity magnitudes are of the order 10^{-5}.

analysis window, the features are maintained over the 5 days by adjustments to the wind stress forcing. Wind stress increments display an increase in onshore wind stress to the south of the COFFS domain and an increase in offshore wind stress to the north on average (Fig. 8c and d). These adjustments allow the analysis to better represent the cyclonic band inshore of the EAC and achieve greater cyclonic vorticity over the shelf slope on average (as discussed in the following section).

3.3. Vorticity

We are interested in understanding the predictability inshore of the EAC jet, where the flow is more variable due to the formation and evolution of frontal eddies. Ocean surface vorticity describes the local rotation and is given by $\zeta = \delta v/\delta x - \delta u/\delta y$, where v and u are the meridional and zonal velocity components. A positive (negative) vorticity indicates anti-clockwise (clockwise) rotation. Here we compute the surface vorticity from the modelled surface velocity fields every 4 h, and present the time-mean and standard deviations of surface vorticity. The EAC analyses (Fig. 9a) show anti-clockwise (anti-cyclonic) vorticity offshore of the 1000 m bathymetry contour, where EAC flows poleward and separates from the coast, and clockwise (cyclonic) vorticity over the continental shelf on the inshore edge of the EAC. North of the typical EAC separation zone (~ 32°S), vorticity variability is greatest inshore of the 1000 m contour (Fig. 9b), where frontal eddies form inshore of the EAC jet (e.g. Schaeffer et al., 2017). Poleward of the separation zone the vorticity variability spreads across the region of elevated eddy activity in the Tasman Sea (refer to Fig. 2a). Fig. 9c shows the difference in the time-mean surface vorticity between the EAC analyses and forecasts; the negative values, occurring over the shelf slope inshore of the 1000 m bathymetry contour between 28 and 33° S, indicate greater cyclonic vorticity in the analyses.

Time-mean surface vorticity for the COFFS hindcasts is shown in Fig. 10a, showing cyclonic vorticity inshore of the 1000 m bathymetry contour with the strongest region of negative vorticity centred over the 100 m contour which represents the shelf break. The higher resolution model has greater vorticity variance which suggests stronger and more abundant submesoscale flows. The COFFS hindcast has a stronger negative mean surface vorticity inshore of the 1000 m contour compared to the EAC model (Fig. 9a) and the standard deviation of surface vorticity over the shelf break and slope is a factor of two higher for the COFFS hindcast compared to the EAC analysis (compare Figs. 10b and 9b, noting the different colour bar scales).

The vorticity difference between the COFFS hindcast and the COFFS forecasts (Fig. 10c) shows an increase in cyclonic vorticity over the continental slope in the hindcast. This increase in cyclonic vorticity inshore of the EAC jet in the COFFS hindcasts (compared to the COFFS forecasts) is entirely driven by the boundary conditions from the EAC analysis, as no surface forcing adjustment is applied to the COFFS model.

The difference in vorticity between the COFFS forecasts and the EAC forecasts (Fig. 10d) shows that downscaling has a significant effect on vorticity. The higher resolution COFFS model performs better at representing the cyclonic band inshore of the EAC, in comparison to the coarser EAC model, with an increase in cyclonic vorticity along the shelf break, particularly in the northern portion of the COFFS domain, and more anticyclonic(or less cyclonic) rotation on the shelf in the downscaled forecasts on average.

The increased strength and variance of vorticity in the COFFS model compared to the EAC model can be seen in Fig. 11, which illustrates the influence of model resolution on surface vorticity representation for three chosen scenarios when eddies occur inshore of the EAC (described in Section 3.4 below). Relative surface vorticity ($\zeta/|f|$) is plotted for the EAC analysis (panels a–c) and for the corresponding times in the COFFS hindcast (panels d–f) illustrating the stronger vorticity and increased flow structure represented by the COFFS model.

3.4. Eddies inshore of the EAC

A comprehensive characterisation of eddies that form inshore of the EAC, observed by the HF radar, was presented in Schaeffer et al. (2017). Over a one-year period (from 14 September 2012 to 31 September 2013) they find 40 cyclonic eddies, with an eddy forming on average every 7 days (taking data gaps into account) and an average persistence under the HF radar footprint of 28 h. The eddy characteristics are outlined in the supporting information that accompanies their paper. Of the 40 eddies Schaeffer et al. (2017) identified, 27 of them are present in the EAC analysis, while the remaining 13 are not represented as the daily-averaging of the radial observations filters out the short-lived eddy events.

While a detailed analysis and characterisation of all eddies over the

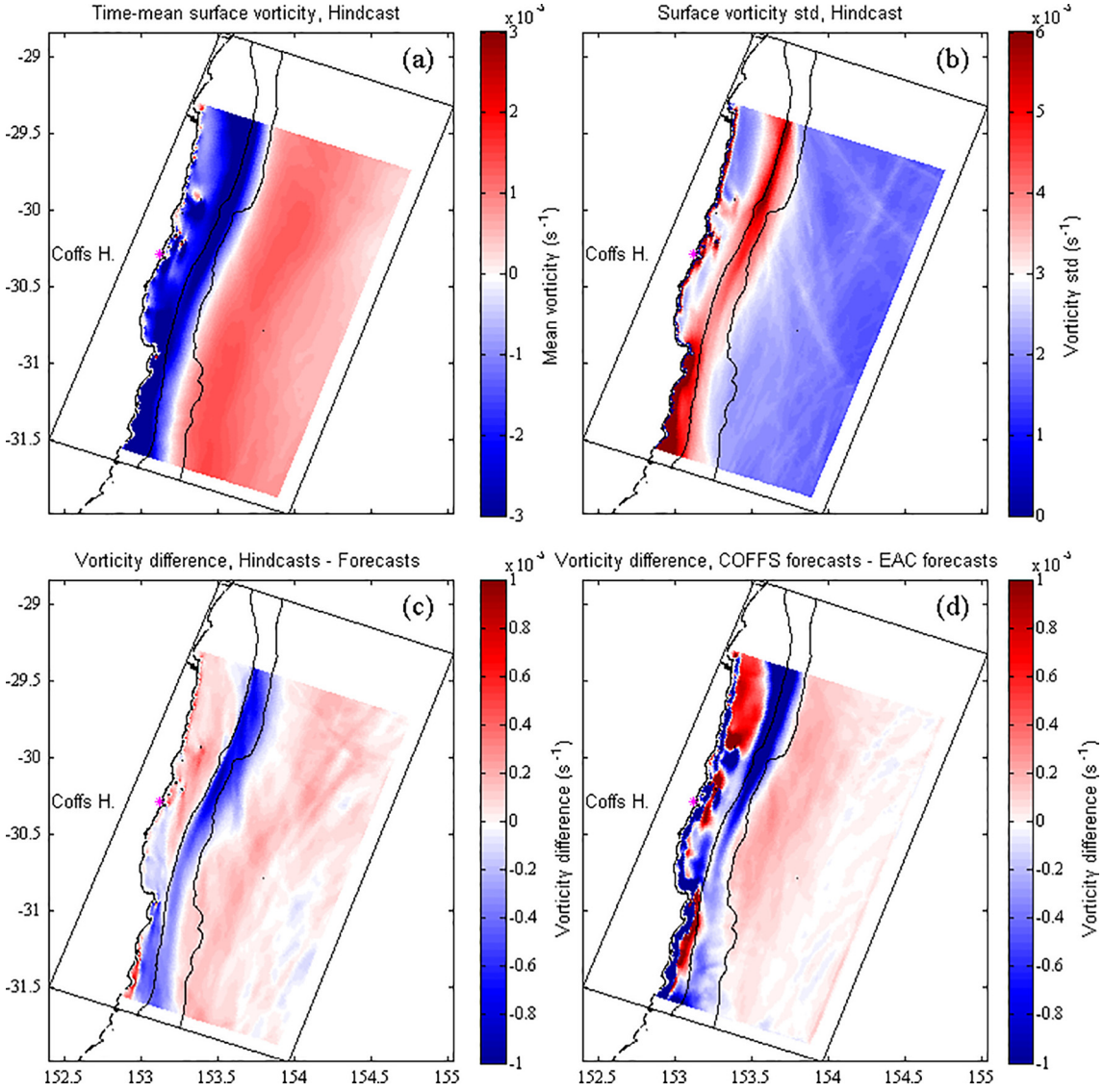

Fig. 10. Time-mean surface vorticity from the COFFS hindcasts (a), standard deviation of surface vorticity computed from 4-hourly averages of hourly snapshots from the COFFS hindcasts (b), time-mean surface vorticity difference between the COFFS hindcasts and COFFS forecasts (c) and time-mean surface vorticity difference between the COFFS forecasts and the EAC forecasts (d). The 100 m and 1000 m COFFS model bathymetry contours are shown (black lines). The plots exclude 10 grid cells inside of the eastern and southern boundaries (the sponge layer) and 60 grid cells from the northern boundary (the sponge layer is 30 grid cells wide here but 60 grid cells are required for the bathymetric merging between the EAC model and the COFFS model). Vorticity magnitudes are of the order 10^{-5}.

2-year period of our modelling study is beyond the scope of this paper, we have chosen three specific scenarios to illustrate the representation of eddies inshore of the EAC in the models. The scenarios describe eddies each with different characteristics and represent 1). A relatively large eddy that is present at the beginning of the forecast period, 2). A smaller recirculation feature that forms during the forecast period, and 3). A frontal eddy that is present at the beginning of the forecast period. The eddies are all characterised by flows with Rossby numbers > 1 (Figs. 12, 14, 16, bottom right panel). To describe the eddy size we define the eddy centre and measure the distance inshore (west) and offshore (east) to the furthest closed streamline, to give both an inshore and offshore radius.

3.4.1. Scenario 1

On March 21 2012, a relatively large eddy is present under the HF radar footprint (Fig. 12) with an inshore (offshore) radius of 45 km (24 km). The frontal eddy is located inshore of an offshore meander of the EAC (flowing poleward at ~2 ms^{-1}) that reattaches to the coast south of the eddy. The eddy's associated flows have Rossby numbers of order 0.5–1.5 along its eastern edge and Richardson numbers of < 1 between the EAC and the eddy (Fig. 12 e–f). March 21 falls on the fourth day of its 5-day forecast/analysis window.

On the first day of the forecast/analysis windows (March 18, Fig. 13 left column) the eddy is of similar size and to the north of its position 3 days later, and the structure is well represented in the EAC and COFFS forecast initial conditions. On day 2 of the window, the northward flow on the inshore edge of the eddy is weaker in the EAC and COFFS forecasts compared to the analysis and hindcast (~0.6 ms^{-1}), however it is slightly better represented in the COFFS forecast (~0.45 ms^{-1} compared to ~0.3 ms^{-1}). Towards day 4 of the forecast window (Mar 21, Fig. 13 right column) the northward flow on the inshore edge of the eddy is ~0.5 ms^{-1}. In the forecasts, the northward flow is considerably dampened in the EAC model (~0.2 ms^{-1}) compared to in the COFFS forecast (~0.35 ms^{-1}). This scenario provides and example of an eddy that is present at the beginning of the forecast window and remains better represented over the length of the window by the higher resolution (COFFS) model compared to the coarser (EAC) model.

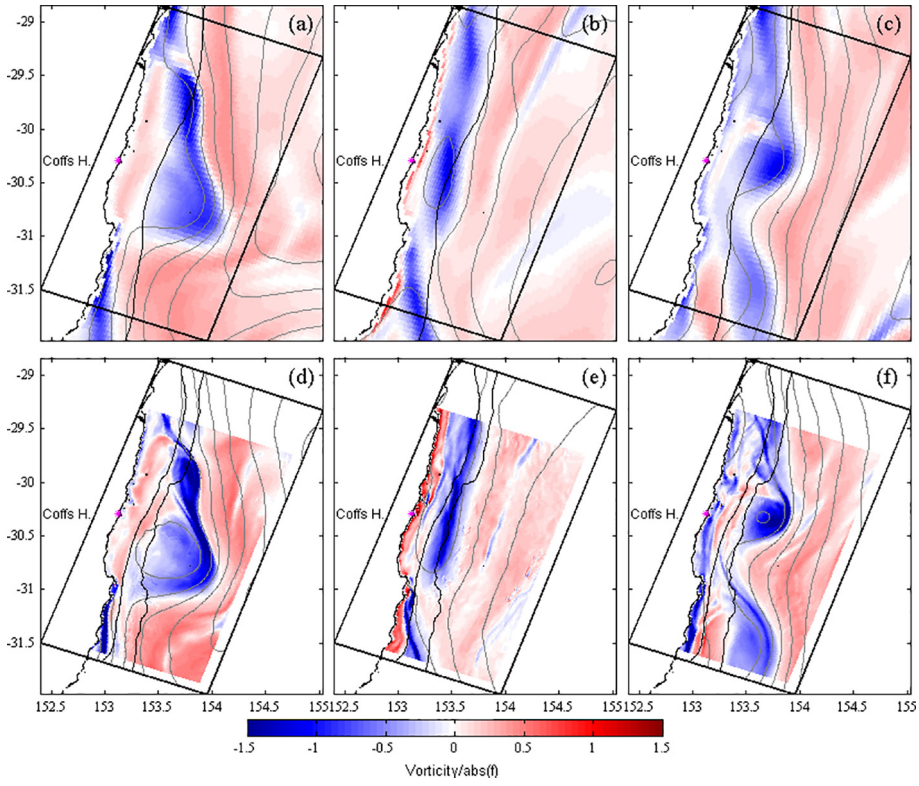

Fig. 11. Relative surface vorticity ($\zeta/|f|$) snapshots for 21 Mar 2012 (EACmodel, a, and COFFS model, d), 15 May 2012 (EACmodel, b, and COFFS model, e), and 29 Jul 2013 (EACmodel, c, and COFFS model, f). The bold black box shows the boundaries of the COFFS model domain. The 1000 m model bathymetry contour is shown for the EAC model (a–c, black lines) and the 100 m and 1000 m model bathymetry contours are shown for the COFFS model (d–f, black lines). SSH contours are every 0.1 m (grey lines). Note that the SSH magnitudes differ for the EAC and COFFS domain as COFFS includes the tides. The plots of the COFFS domain (d–f) exclude 10 grid cells inside of the eastern and southern boundaries (the sponge layer) and 60 grid cells from the northern boundary (the sponge layer is 30 grid cells wide here but 60 grid cells are required for the bathymetric merging between the EAC model and the COFFS model).

3.4.2. Scenario 2

The second scenario presents a smaller feature that forms during a forecast period. On May 14 to 15, 2012, a small, anisotropic and relatively weak frontal eddy forms inshore of the EAC under the HF radar footprint (Fig. 14). It has an inshore (offshore) radius of 9 km (7 km) with an elongated alongshore dimension. High Rossby numbers (> 1) occur along the entire inshore edge of the EAC and Richardson numbers are of O(1) across the eddy (Fig. 14 e–f). In this scenario the EAC partially separates from the coast just downstream of the COFFS domain's southern boundary. May 15 falls on the third day of its 5-day forecast/analysis window.

At the beginning of the corresponding forecast/analysis window (May 13, Fig. 15 left column) the EAC flows adjacent to the shelf slope at ~1 ms^{-1}. The southward flow is considerably stronger in the analysis (~1 ms^{-1}) than in the forecast (~0.5–0.6 ms^{-1}, note that the forecast fields at the beginning of the window are extracted from the previous analysis). On May 14 northward flow adjacent to the coast begins to be observed (~0.3 ms^{-1}) and the northward flow strengthens to ~0.55 ms^{-1} on May 15 which is the third day of the forecast/analysis window (Fig. 15 right column). The COFFS hindcast reproduces the same inshore flow as the EAC analysis (which is also present in the observations, not shown). The feature is not reproduced in the EAC forecast, and while a weak northward flow does develop in the COFFS forecast (~0.25 ms^{-1} on May 15) it is much weaker than the observed feature.

3.4.3. Scenario 3

The third scenario takes place on July 29 2013 when the EAC flows at ~1.5 ms^{-1} as a coherent poleward jet along the edge of the shelf slope before separating from the coast at about 34°S (Fig. 16). The EAC meanders off Coffs Harbour and a frontal eddy is present at its inshore edge at 30.3°S with an inshore (offshore) radius of 19 km (12 km). As seen in Fig. 16 this eddy is characterised by high Rossby numbers (> 1, panel f) and low Richardson numbers (of O(1), panel e), particularly across its eastern side adjacent to the EAC. A submesoscale billow is also present to the south at 31.5°S. July 29 falls on the third day of its 5-day forecast/analysis window. July 29 falls on the fourth day of its 5-day forecast/analysis window.

At the beginning of the forecast/analysis window (July 26, Fig. 17, left columns) there is northward flow inshore of the strong (~1.5 ms^{-1}) EAC jet and a single cyclonic feature evident in the SSH fields. This northward flow is underestimated in the COFFS and EAC model forecast initial conditions. On day 2 of the window this single feature persists in the model forecasts, although it moves a little offshore as the northward flow on its inshore edge strengthens (from ~0.4 ms^{-1} to ~0.55 ms^{-1}). In the observations however, and hence the analysis and hindcast, two distinct frontal eddies become present. These eddies strengthen and migrate southward over the next few days, and are seen in the analysis and hindcast fields on July 29 (Fig. 17, right columns). Frontal eddies also evolve in the forecasts but the forecast models do not correctly represent the location and size of the observed eddies. In this scenario, the northward flow (cyclonic vorticity) is stronger in the COFFS forecast compared to the EAC forecast, even though neither correctly predict the frontal eddy formation and evolution.

The larger eddy that is present at the beginning of the forecast period (Scenario 1) remains better represented over the length of the window by the higher resolution (COFFS) model compared to the coarser (EAC) model. The smaller recirculation feature that forms during the forecast period (Scenario 2) is not reproduced in the EAC forecast, and while a weak northward flow does develop in the COFFS forecast it is much weaker than the observed feature. The smaller frontal eddy that is present at the beginning of the forecast period (Scenario 3) does not evolve with the correct timing and location in either of the forecasts. While these scenarios provide interesting examples of the representation and evolution of three specific eddies in the model, more detailed analysis of the evolution of the eddies inshore of the EAC over the 2-year period is required.

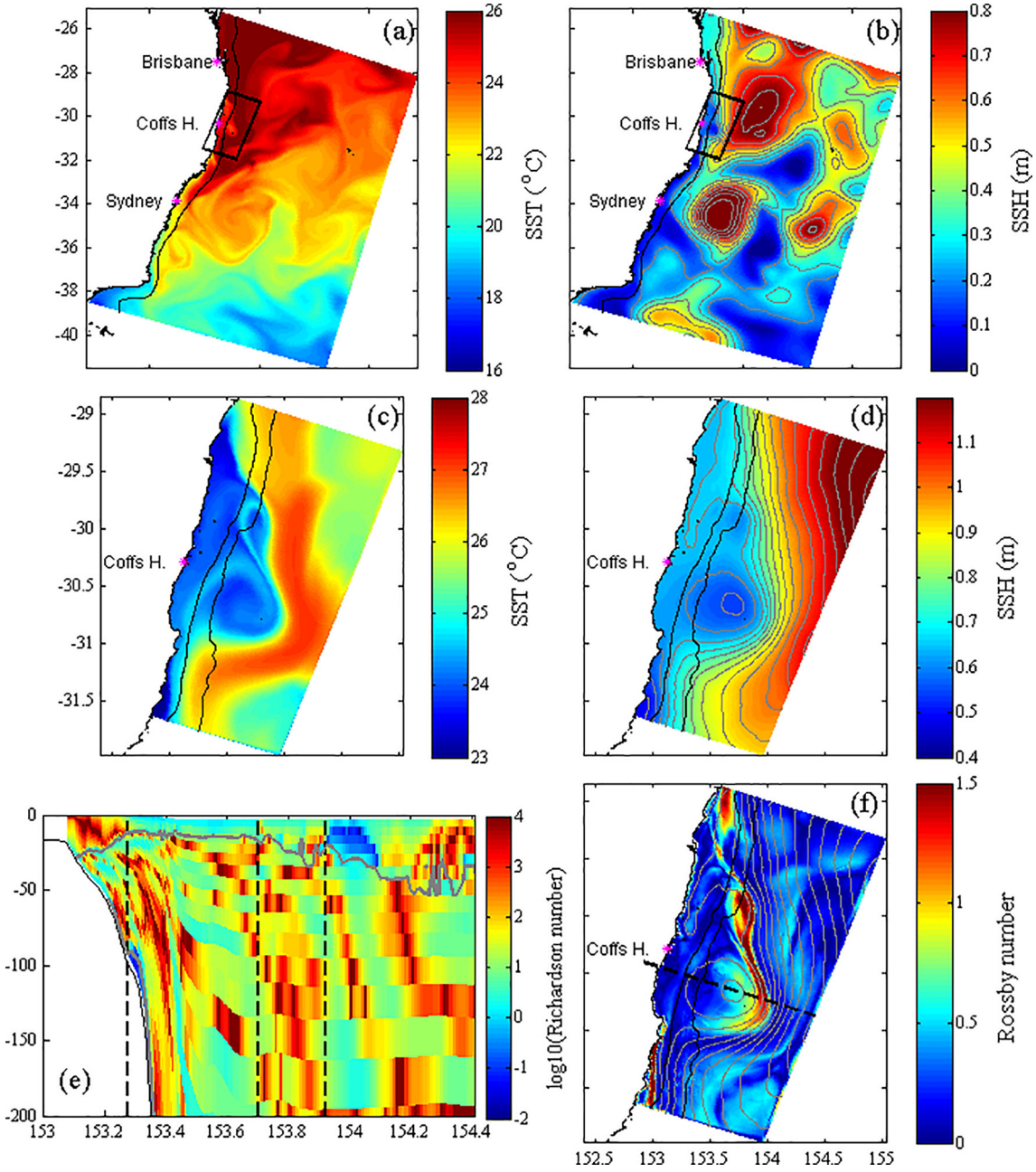

Fig. 12. Instantaneous SST, SSH, Ri and Ro numbers on 21 March 2012 from the models. SST (a) and SSH (b) from the EAC analysis and SST (c) and SSH (d) from the COFFS hindcast. The 1000 m model bathymetry contour is shown for the EAC domain (a and b, black line) and SSH contours are every 0.1 m (grey lines). For the COFFS domain (c and d), the 100 m and 1000 m model bathymetry contours are shown (black lines) and the SSH contours are every 0.05 m (grey lines). Note that the SSH magnitudes differ for the EAC and COFFS domain as COFFS includes the tides. Ri number for the COFFS hindcast (e) through the section shown by the black dashed line in (f). The vertical black dashed lines show the inshore, centre, and offshore extent of the eddy, and the grey line depicts Ri = 1. Ro number for the COFFS hindcast (f).

4. Discussion

4.1. Growth of uncertainty in the coastal (COFFS) model

Model forecast errors can arise from uncertainties in initial conditions, boundary and surface forcings, imperfect model physics, and errors of representativeness. Errors of representativeness relate to the representation of the ocean state as a discretised model in space and time, in which unresolved, sub-grid scale processes must be parameterised. During the initial period, the forecast depends mostly upon the initial conditions; however, as the forecast length grows, model error dominates the forecast skill. Model error can be separated into forcing error, originating from errors in the boundary and surface forcing, and internal model error, stemming from the growth of uncertainties within the model due to imperfect model physics, parameterisations and errors of representativeness (e.g. model resolution). Our results show that error growth in the coastal (COFFS) forecasts is due to error in the boundary forcing from the regional (EAC) model, with internal model error having a smaller effect.

The COFFS hindcasts, which take initial conditions and boundary forcing from the corresponding EAC analysis, show inferior agreement with the SST observations and temperature and velocity observations from the moorings, compared to the EAC analyses that assimilate these observations (Fig. 5). This inferior agreement may be due to internal

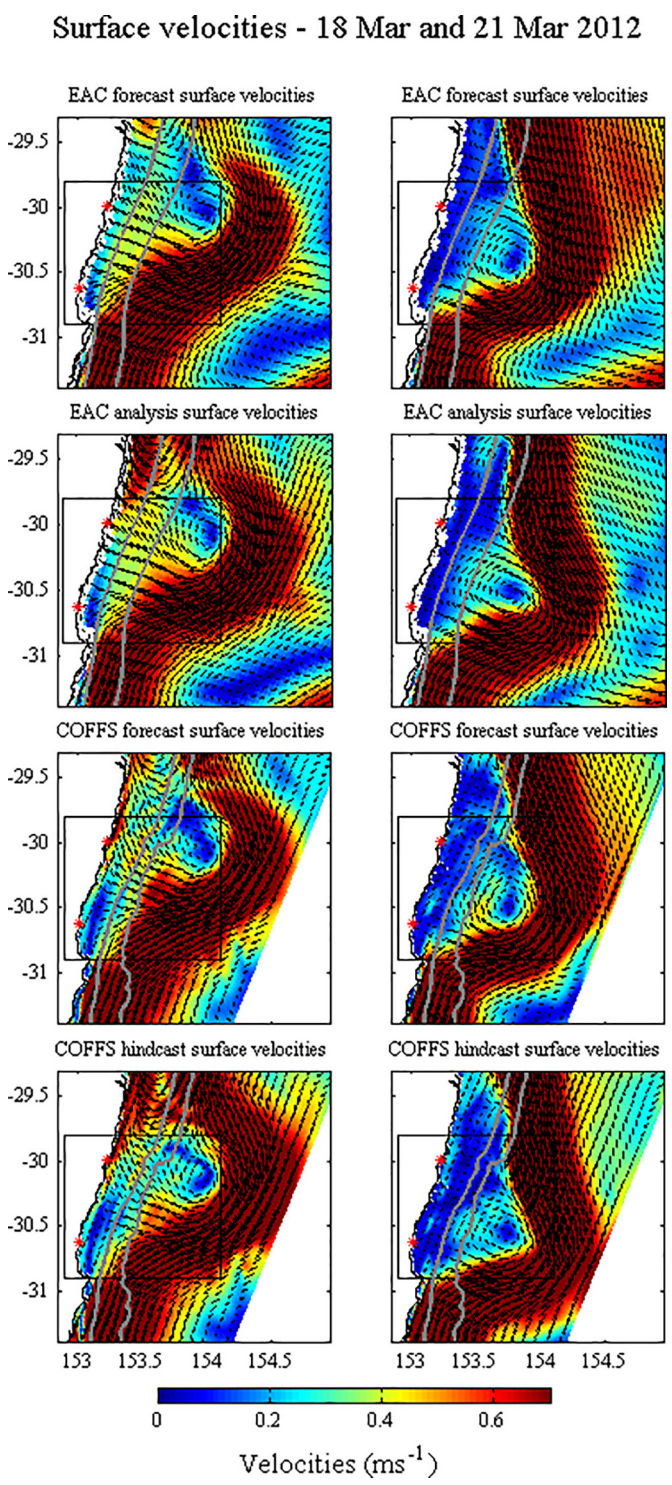

Fig. 13. Instantaneous velocity fields on 18 March and 21 March 2012 (days 1 and 4 of the 5-day window). The black box shows the approximate region of HF radar coverage. The 100 m and 1000 m model bathymetry contours are shown (grey lines).

model error, causing deviation of the flow from that represented by the analysis, and from errors in the representation of high-frequency processes such as the tides and inertial oscillations, which are filtered out of the EAC model and observations. While internal errors would grow in time over the 5-day window, misrepresentation of the high-frequency processes would likely be fairly constant over the 5 days. The surface velocity complex correlations for the COFFS hindcasts (Fig. 6, row c) remain fairly constant over the 5 days indicating that the boundaries, provided by the EAC analyses, play a dominant role in constraining the surface velocity field and internal error has a relatively small effect.

The growth of uncertainty in the COFFS forecasts depends on two main factors; the forcing error, which is dominated by uncertainty in the boundaries and increases over the 5-day window as error in EAC forecast grows; and the internal model error within the COFFS model. The EAC forecasts and the COFFS forecasts show agreement of similar magnitude for SST and temperature and velocity mooring observations (Fig. 5). It is likely that the errors in representation of the high-frequency processes (such as tides and inertial oscillations), which would result in higher errors in the COFFS forecasts compared to the EAC forecasts, are counteracted by the higher resolution COFFS forecasts providing better representation of the lower frequency processes (such as the frontal eddies) than the coarser EAC model. This improved representation of the lower frequency processes is supported by the improved representation of cyclonic vorticity along the continental shelf slope, on average, in the COFFS forecasts compared to the EAC forecasts (Fig. 10d).

As the COFFS forecast surface velocity comparisons progress over the 5-day windows (Fig. 6, row d), the region of highly correlated velocities (> 0.9) narrows in the cross-shore direction. The degradation in surface velocity agreement over the 5-day windows in the COFFS forecast is similar to that in the EAC forecast (Fig. 6, row b), consistent with the suggestion that, for the COFFS model, the boundary forcing errors dominate over internally-generated model errors. The region that remains highly correlated after 5 days corresponds to the region of strong poleward velocity in the mean, over which the velocity variance ellipses have a small cross-shore component and are aligned with the mean flow (refer to Fig. 3 of Archer et al., 2017). Inshore and offshore of the typical location of the EAC jet, surface velocity predictability is less.

The dominant influence of the boundary forcing on the COFFS model skill is further supported by inspection of the scenarios (Section 3.4, Figs. 12– 17). The frontal eddies observed under the HF radar footprint are well represented in the EAC analyses upon assimilation of the daily-averaged surface radial velocity measurements, and the COFFS hindcasts also provide very good representation of these features even towards the end of the hindcast windows. Specifically, refer to Figs. 15 and 17 where the generation and evolution of submesoscale frontal eddies that are not present at the beginning of the window are well represented over the COFFS hindcast period.

4.2. Vorticity

The submesoscale features that form along the inshore edge of the EAC grow from instabilities of the jet. The growth rate of these instabilities depends on the vorticity structure of the jet. Resolving the dynamics of the inshore cyclonic band of the jet may be the key to allow submesoscale features to grow. The representation of vorticity along the inshore edge of the EAC in the prediction system is influenced by both data assimilation of surface velocities at the regional (EAC) model level and downscaling to a higher resolution (COFFS) model.

Assimilation of surface radial velocities from the HF radar array in the regional (EAC) model results in greater cyclonic vorticity over the shelf slope inshore of the 1000 m bathymetry contour in the analyses compared to the forecasts (Fig. 9c). This is achieved by adjustments to both the velocity initial conditions and the wind stress forcing (Fig. 8) to increase the cyclonic vorticity of the modelled circulation over the continental shelf slope to better match the observed velocity field. The increment adjustments reveal that the EAC model performs poorly at maintaining the sharp cyclonic band inshore of the EAC in forecast mode. Wind forcing is however unlikely to play a significant role in the inshore cyclonic band or the generation or evolution of most of the cyclonic eddies inshore of the EAC (Schaeffer et al., 2017). While it has been suggested that northward winds opposing the EAC flow may drive

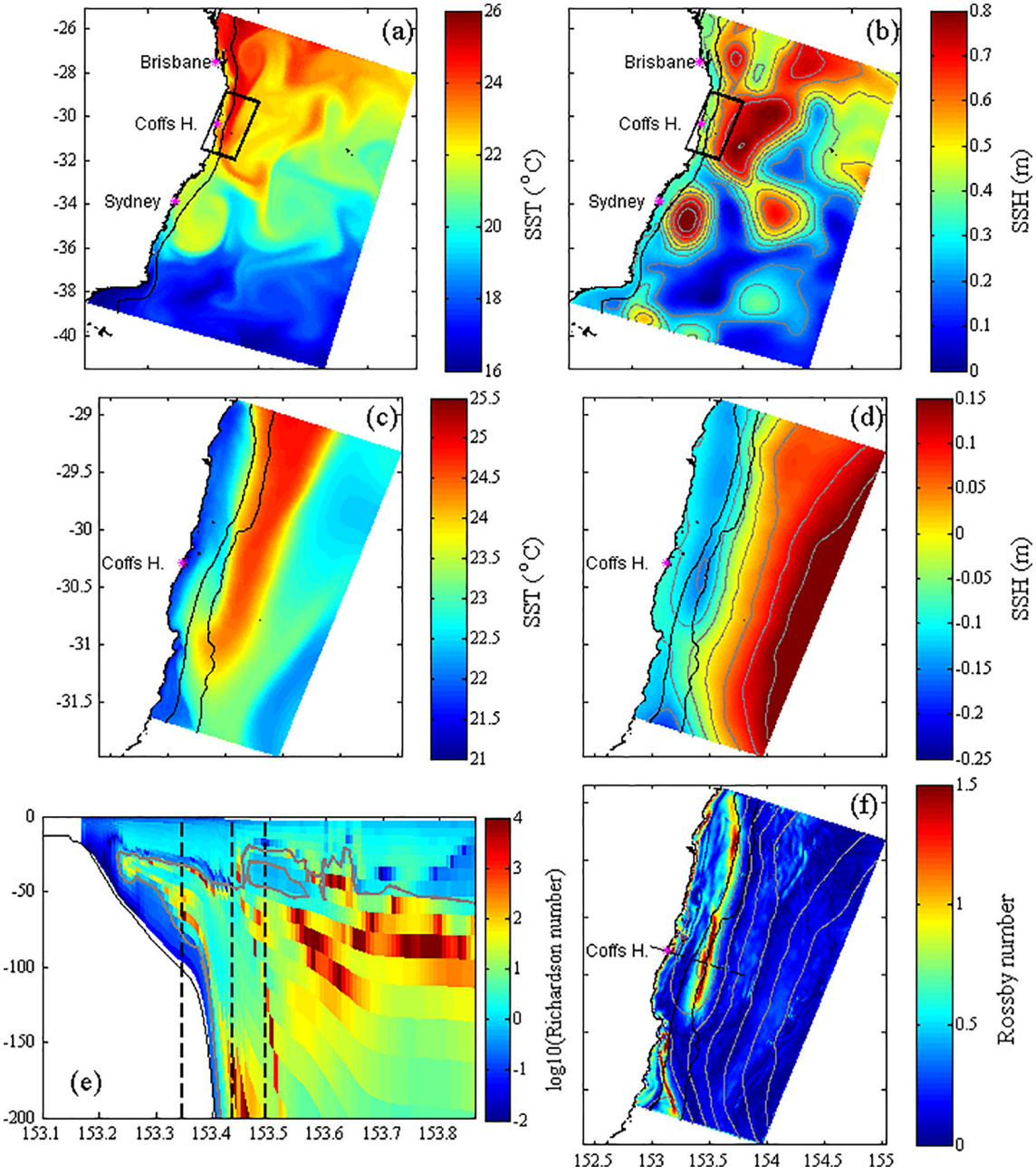

Fig. 14. Instantaneous SST, SSH, Ri and Ro numbers on 15 May 2012 from the models. SST (a) and SSH (b) from the EAC analysis and SST (c) and SSH (d) from the COFFS hindcast. The 1000 m model bathymetry contour is shown for the EAC domain (a and b, black line) and SSH contours are every 0.1 m (grey lines). For the COFFS domain (c and d), the 100 m and 1000 m model bathymetry contours are shown (black lines) and the SSH contours are every 0.05 m (grey lines). Note that the SSH magnitudes differ for the EAC and COFFS domain as COFFS includes the tides. Ri number for the COFFS hindcast (e) through the section shown by the black dashed line in (f). The vertical black dashed lines show the inshore, centre, and offshore extent of the eddy, and the grey line depicts Ri = 1. Ro number for the COFFS hindcast (f).

frontal destabilisation (Mantovanelli et al., 2017) and may stall the southward displacement of some frontal eddies (Schaeffer et al., 2017), the increased cyclonic vorticity of the winds imposed by the surface forcing adjustments are mostly unrealistic drivers of the cyclonic band inshore of the EAC. The unrealistic nature of the increment adjustments reveals the inability of the regional (2.5 –6 km resolution) EAC model to reproduce the sharp vorticity gradient observed by the HF radar. Increasing the horizontal length scales prescribed to the atmospheric forcing in the background error covariance matrix would preclude these unrealistic adjustments and likely result in an inferior fit between the reanalysis and the surface velocity observations.

Downscaling to a higher resolution coastal (COFFS) model produces a sharper across-current vorticity gradient within the EAC, with greater cyclonic vorticity along the shelf break where the vorticity minimum is centred on the 1000 m isobath. The inshore cyclonic band of the jet is wider and more intense within the high resolution model. This leads to increased values of surface vorticity variance inshore of the EAC in the high resolution model as the better representation of the vorticity structure of the jet allows small scale instabilities to grow. Nesting the high resolution (COFFS) model inside the EAC analysis (the COFFS hindcast) produces a sharper gradient of vorticity inside the jet, limits the cross-shore extension of the jet to the shelf break, and leads in turn to more intense submesoscale features growing on the inshore side of the EAC. The COFFS hindcast has a stronger negative mean surface

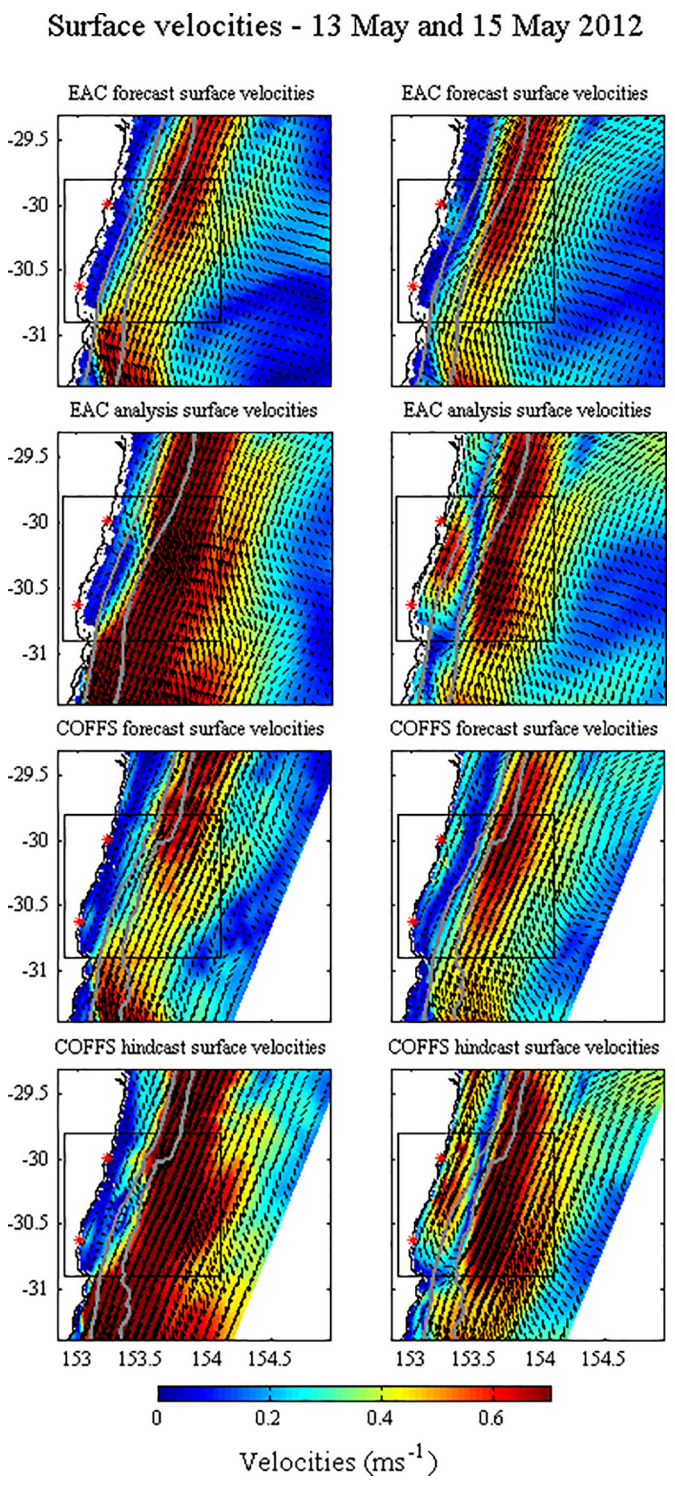

Fig. 15. Instantaneous velocity fields on 13 May and 15 May 2012 (days 1 and 3 of the 5-day window). The black box shows the approximate region of HF radar coverage and the bounds of the observation plots. The 100 m and 1000 m model bathymetry contours are shown (grey lines).

vorticity inshore of the 1000 m contour compared to the EAC analysis (Fig. 9a) and the standard deviation of surface vorticity over the shelf break and slope is a factor of two higher for the COFFS hindcast.

In forecast mode, downscaling results in better representation of the cyclonic band inshore of the EAC (Fig. 10d). The COFFS forecasts receive boundary conditions from the EAC forecasts, so the increase in cyclonic vorticity results from improved representation of the circulation dynamics by resolving smaller spatial scales. In addition, increased bathymetric resolution resulting in a sharper transition between continental shelf and slope in the COFFS model (Fig. 2c) is likely to result in concentration of the negative vorticity over the shelf break location in the COFFS model, with less cyclonic vorticity inshore over the shelf.

In future work we hope to assimilate radial velocities at higher temporal resolution in order to capture the short-lived eddies that form inshore of the EAC. For the EAC analysis, a 24-hour boxcar filter was applied to the radial velocities to filter out tides and inertial oscillations which was considered appropriate as the EAC model was designed to study mesoscale flows. An eddy tracking algorithm could be used to investigate in more detail the ability of the model to predict the evolution of the frontal eddies.

4.3. Improving prediction of fine-scale features

Mesoscale flows are slowly-evolving (on the order of weeks to months) and so mesoscale predictability on time scales of days to a week is highly sensitive to the initial state. Effective mesoscale forecasting systems use data assimilation techniques to reduce the residuals between model output and observations to minimise the error in the initial state at the beginning of each forecast window, and much effort has been put into improving these methods to provide improved state estimates and thus improved forecasts. This works effectively for mesoscale forecasting in the regional EAC model (Roughan et al., 2018).

Fine-scale flows, such as submesoscale eddies, are more rapidly-evolving (with typical lifetimes on the order of a few days, e.g. Schaeffer et al., 2017), so their prediction presents additional challenges. The circulation is more quickly decoupled from the initial state and model error dominates more rapidly; prediction on time scales of days to a week becomes dependent on the model's ability to represent the dynamics of formation and evolution of the circulation features. Our results show that, while assimilation of surface velocity data corrects the representation of cyclonic band inshore of the EAC in the regional EAC model, the vorticity is not well represented in the regional forecasts due to the coarse model resolution. Downscaling to a higher resolution model results in improved representation of vorticity in the forecasts.

Submesoscale flows inshore the EAC are likely to form through growing baroclinic instabilities in the mixed layer (Schaeffer et al., 2017). These instabilities can develop at horizontal scales of the order of the internal Rossby radius of deformation of the mixed layer, given by $L_d = NH/f$, where N is the density stratification in the mixed layer, H is its depth and f is the Coriolis parameter. The most unstable mode has a wavelength of about $3.9L_d$ and a growth rate of $0.3f\Lambda/N$, where Λ is the geostrophic shear in the mixed layer (Lindzen and Farrell, 1980; Vallis, 2006). Given mixed layer depths of about 50 m in summer to 100–150 m in winter (Condie and Dunn, 2006 and computed from the EAC model) and typical values of $N \sim 10^{-3}s^{-1}$, $\Lambda \sim 10^{-4}s^{-1}$, and f at 30°S of $7.3 \times 10^{-5}s^{-1}$, the mixed layer Rossby radius of deformation ranges from about 650 m in summer to 2 km in winter. Baroclinic instability disturbances would therefore grow on horizontal scales of 2.5–8 km and time scales of the order of a few days. In order to predict mixed layer baroclinic instabilities, a model must therefore resolve the Rossby radius of deformation in the mixed layer. The dependence of the season on predictive skill is a subject for further study.

Clearly the EAC model, at 2.5–5 km resolution over the continental shelf and slope does not adequately resolve these horizontal scales. The COFFS model, at 750 m–1 km resolution resolves the scales of mixed layer baroclinic instabilities in winter ($L_d \sim$2 km), but may fall short in summer ($L_d \sim$650 m) when the mixed layer shallows. Several modelling studies have found that increasing grid resolution towards the submesoscale results in stronger and more abundant submesoscale eddies and vorticity filaments (Bracco et al., 2016, 2018; Gula et al., 2016; Lévy et al., 2001; Luo et al., 2016; Zhong and Bracco, 2013), as well as

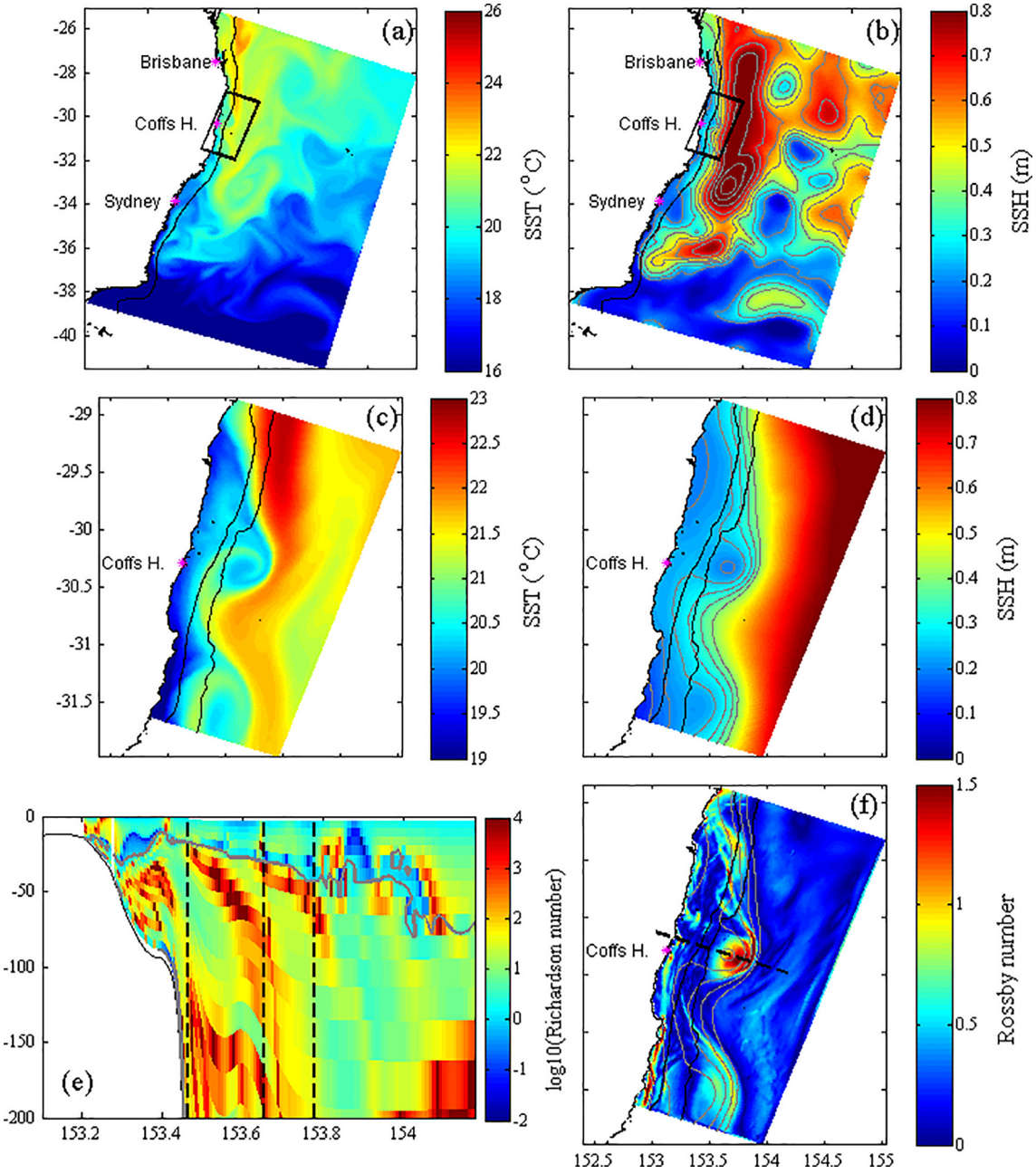

Fig. 16. Instantaneous SST, SSH, Ri and Ro numbers on 29 July 2013 from the models. SST (a) and SSH (b) from the EAC analysis and SST (c) and SSH (d) from the COFFS hindcast. The 1000 m model bathymetry contour is shown for the EAC domain (a and b, black line) and SSH contours are every 0.1 m (grey lines). For the COFFS domain (c and d), the 100 m and 1000 m model bathymetry contours are shown (black lines) and the SSH contours are every 0.05 m (grey lines). Note that the SSH magnitudes differ for the EAC and COFFS domain as COFFS includes the tides. Ri number for the COFFS hindcast (e) through the section shown by the black dashed line in (f). The vertical black dashed lines show the inshore, centre, and offshore extent of the eddy, and the grey line depicts Ri = 1. Ro number for the COFFS hindcast (f).

improved representation of large-scale horizontal flows (Chassignet and Xu, 2017; Lévy et al., 2010). In this work we find that downscaling to the higher resolution COFFS model (750 m–1 km) results in an increase in cyclonic vorticity estimates along the continental shelf slope inshore of the EAC on average (Fig. 10d), associated with greater vorticity variance due to stronger and more abundant submesoscale features (e.g. Fig. 11). While more detailed analysis of the evolution of specific frontal eddies is required, Scenario 3 in Section 3.4.3 suggests that the frontal eddies do not always form or evolve with the correct timing or location in the forecasts.

Vertical resolution is also important to model submesoscale flows (e.g. Bracco et al., 2018). While our models have sufficient vertical resolution to resolve the first baroclinic mode (Stewart et al., 2017), the sensitivity to vertical resolution was not studied in this work.

While the strength and abundance of submesoscale features have a strong dependence on model resolution, the prediction of submesoscale forming instabilities is likely highly dependent on model parameterisations. Associated with the chosen parameterisation schemes, advanced ocean models contain many parameters that have a significant effect on the predictive capability. Indeed, Zou et al. (1992) suggest that model error (of atmospheric models) is primarily due to parameterisations of the model physics (such as prior specifications of mixing coefficients, viscosity etc.). While the sensitivity of model forecasts to parameters was not explored in this study, we propose that

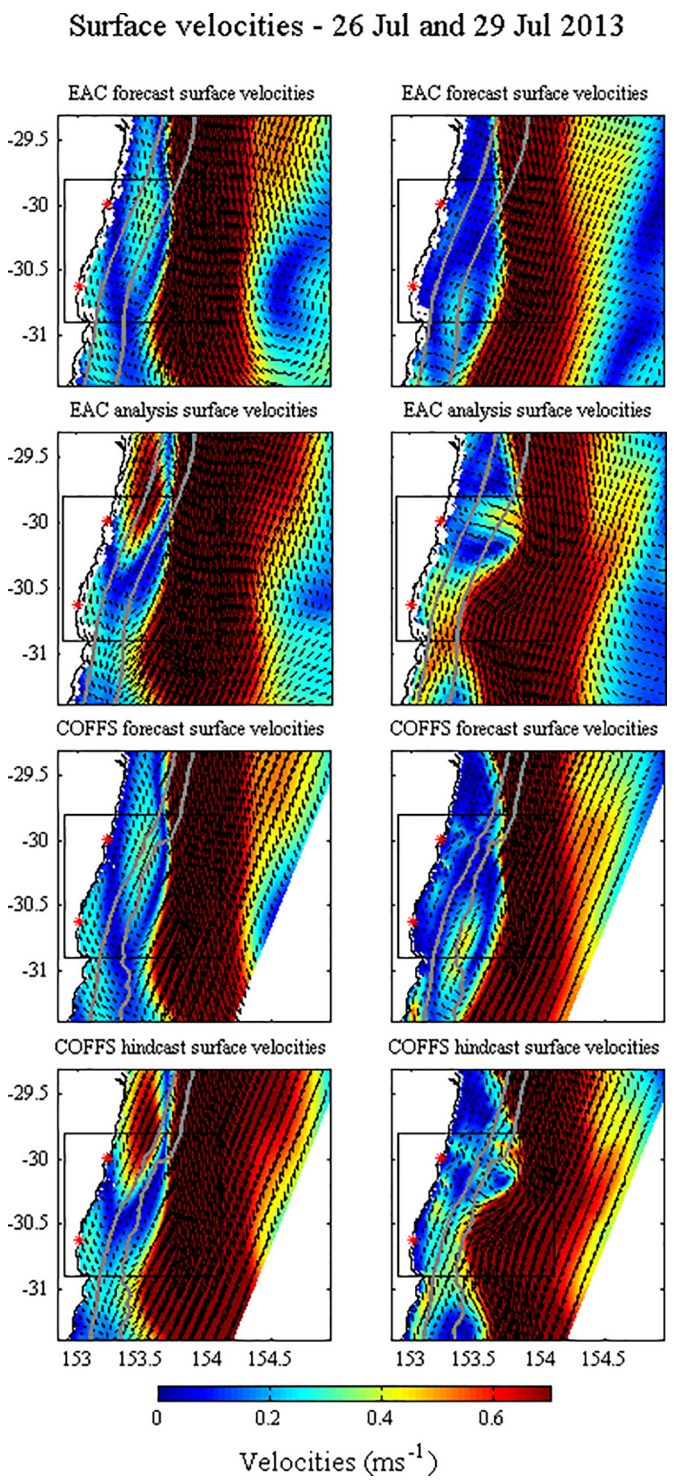

Fig. 17. Instantaneous velocity fields on 27 July 2013 and 29 July 2013 (days 1 and 3 of the 5-day window). The black box shows the approximate region of HF radar coverage. The 100 m and 1000 m model bathymetry contours are shown (grey lines).

optimisation of a selection of meaningful parameters in the EAC model, through their inclusion in the control vector, may be useful in improving the predictive skill of eddy-forming instabilities. Two-way nesting may also improve the prediction of the more rapidly-evolving submesoscale flows at the regional level, and this approach demands further investigation.

Our results show that error growth in the coastal (COFFS) forecasts stems from error in the boundary forcing from the regional (EAC) model (discussed in Section 4.1). While our results suggest that downscaling to a higher resolution model provides improved representation of the vorticity variance associated with submesoscale flows inshore of the EAC, accurate prediction of the timing and location of submesoscale features requires improved prediction of the more rapidly-evolving submesoscale flows at the regional level to provide boundary conditions for coastal downscaling. To achieve this, effort must be focussed on reducing internal model error in the regional forecasts.

More research is required on the impact of increased model resolution and the choice of model parameterisation on the predictions of submesoscale and mesoscale flows. Sandery and Sakov (2017) found that increasing model resolution towards the submesocale (2.5 km from 10 km) for an Ensemble Optimal Interpolation (EnOI) data assimilation system resulted in deterioration of forecast skill of mesoscale features in the EAC system. They suggest that resolving the less predictable submesoscale lowers the predictability of the mesoscale as there is an inverse cascade in the kinetic energy spectrum.

5. Conclusions

There is an increasing demand for improved prediction of submesoscale flows and this study focuses on the predictability of the fine-scale circulation inshore of the EAC. We present the capacity of an operational system to reproduce inshore coastal submesoscale features by downscaling a regional mesoscale eddy-resolving model that is data-constrained. Resolving the cyclonic band of vorticity is key to predicting fine-scale flows inshore of the EAC, as small-scale instabilities grow on the inshore side of this vorticity minimum. We show that assimilation of surface radial velocities from a HF radar array into a regional model (2.5–6 km resolution) of the EAC region provides a more pronounced across-shore vorticity structure inshore of the EAC. However the increment adjustments made to the model surface forcing to achieve this are unrealistic, revealing the inability of the regional model to reproduce the sharp vorticity gradient observed by the HF radar. Downscaling to a higher resolution coastal model (750–1000 m resolution) produces an even sharper gradient of vorticity inshore of the EAC and leads in turn to more intense submesoscale features growing on the currents's inshore side. These results highlight the importance of horizontal model resolution in the representation of the submesoscale flows inshore of a WBC.

We find that error growth in the downscaled forecasts is dominated by error in the boundary forcing from the regional forecasts, with internal model error having a smaller effect. While the cyclonic vorticity may be better represented in the higher resolution model, the predictive skill is limited by the introduction of boundary forcing errors from the lower resolution model. The timing and location of submesoscale features, reproduced in the data-constrained model, are not always correctly represented in the forecasts. The results motivate further study into the evolution of submesoscale eddy events in model forecasts and suggest that, in order to predict the timing and location of submesoscale features, effort should be focussed on improved representation of fine-scale flows in regional forecasts for downscaling purposes.

While much effort has focussed on improved estimates of the initial state to improve mesoscale ocean circulation forecasts, to advance submesoscale predictability further research must focus on reducing model error in regional forecasts. It is likely that both increased model resolution and parameter optimisation are required to make progress towards improving the predictive skill of fine-scale flows in regional models. In terms of model resolution, we suggest that knowledge of length scales for eddy-forming instabilities (such as the Rossby radius of deformation of the mixed layer) is important where submesoscale instabilities occur.

The feasibility of increased model resolution at the regional model level is dependent on the available computing infrastructure, and the

influence on mesoscale predictability is unclear (e.g. Sandery and Sakov, 2017). Furthermore, the spatial resolution of observations available at present is insufficient to constrain submesoscale flows. The impending availability of data from the Surface Water and Ocean Topography (SWOT, Desai, 2018) mission, providing high spatial resolution (~1 km) sea surface observations at low temporal resolution (revisit times of ~ 11 days), provides new opportunity for the prediction of submesoscale flows and introduces new challenges to predict the submesoscale flow evolution between observation times.

Indeed predicting the submesoscale is a new frontier and there is much work to be done. These results regarding the predictability of the circulation inshore of the EAC provide motivation for further work in the field. The results are also relevant to analogous WBCs e.g the Kuroshio in the northwestern Pacific and the Gulf Stream adjacent to the US east coast.

Acknowledgements

Dr. C. Kerry was partially supported by ONR Global Award #N62909-17-1-2141. Ocean observational data was primarily sourced from the Integrated Marine Observing System (IMOS) – IMOS is a national collaborative research infrastructure, supported by the Australian Government.

References

Andreu-Burillo, I., Brassington, G., Oke, P., Beggs, H., 2010. Including a new data stream in the BLUElink Ocean Data Assimilation System. Aust. Meteorol. Ocean. 59, 77–86.
Archer, M., Roughan, M., Keating, S., Schaeffer, A., 2017. On the variability of the East Australian Current: jet structure, meandering, and influence on shelf circulation. J. Geophys. Res. Oceans 122, 1–18.
Berliand, M.E., Berliand, T.G., 1952. Measurements of the effective radiation of the Earth with varying cloud amounts (in Russian). Izv. Akad. Nauk. SSSR Ser. Geogr. I.
Bracco, A., Choi, J., Joshi, K., Luo, H., McWilliams, J.C., 2016. Submesoscale currents in the northern Gulf of Mexico: deep phenomena and dispersion over the continental slope. Ocean Model. 101, 43–58.
Bracco, A., Choi, J., Kurian, J., Chang, P., 2018. Vertical and horizontal resolution dependency in the model representation of tracer dispersion along the continental slope in the northern Gulf of Mexico. Ocean Model. 122, 13–25.
Callies, J., Ferrari, R., Klymak, J.M., Gula, J., 2015. Seasonality in submesoscale turbulence. Nat. Commun. 6 (6862), 1–8.
Cetina-Heredia, P., Roughan, M., Van Sebille, E., Coleman, M., 2014. Long-term trends in the East Australian Current separation latitude and eddy driven transport. J. Geophys. Res. 119 (May).
Chapman, D.C., 1985. Numerical treatment of cross-shelf open boundaries in a barotropic coastal ocean model. J. Phys. Oceanogr. 15, 1060–1075 (August).
Chassignet, E.P., Xu, X., 2017. Impact of horizontal resolution (1/12° to 1/50°) on gulf stream separation, penetration, and variability. J. Phys. Oceanogr. 47, 1999–2021 (August).
CNES, 2015. SSALTO/DUACS User Handbook: (M)SLA and (M)ADT Near-Real Time and Delayed Time Products. AVISO Sateliitle Altimetry Data.
Condie, S.A., Dunn, J.R., 2006. Seasonal characteristics of the surface mixed layer in the Australasian region: implications for primary production regimes and biogeography. Mar. Freshwater Res. 57, 569–590.
De Souza, J.M.A.C., Powell, B., Castillo-Trujillo, A.C., Flament, P., 2015. The vorticity balance of the ocean surface in Hawaii from a regional reanalysis. J. Phys. Oceanogr. 45, 424–440.
Desai, S., 2018. Surface water and ocean topography mission (SWOT) project; science requirements document. In: Tech. Rep. JPL D-61923. National Aeronautics and Space Administartion, Jet Propulsion Laboratory (January).
Di Lorenzo, E., Moore, A.M., Arango, H.G., Cornuelle, B.D., Miller, A., Powell, B.S., Chua, B.S., Bennett, A.F., 2007. Weak and strong constraint data assimilation in the inverse regional ocean modelling system (ROMS): development and application for a baroclinic coastal upwelling system. Ocean Model. 16, 160–187.
Duda, T.F., Zhang, W.G., Helfrich, K.R., Newhall, A., Lin, Y., Lynch, J.F., Lermusiaux, P.F.J., Haley Jr., P., Wilkin, J., 2014. Issues and Progress in the Prediction of Ocean Submesoscale Features and Internal Waves. OCEANS'14 MTS/IEEE (September).
Egbert, G.D., Erofeeva, S.Y., 2002. Efficient inverse modeling of barotropic ocean tides. J. Atmos. Ocean. Technol. 19, 183–204 (February).
Everett, J.D., Macdonald, H.S., Baird, M.E., Humphries, J., Roughan, M., Suthers, I.M., 2015. Cyclonic entrainment of preconditioned shelf waters into a frontal eddy. J. Geophys. Res. Oceans 120 (2), 677–691.
Fairall, C.W., Bradley, E.F., Rogers, D.P., Edson, J.B., Young, G.S., 1996. Bulk parameterization of air-sea fluxes for tropical ocean-global atmosphere Coupled-Ocean Atmosphere Response Experiment. J. Geophys. Res. 101, 3747–3764.
Flather, R.A., 1976. A tidal model of the northwest European continental shelf. Mem. Soc. R. Sci. Liege 6, 141–164.
Gula, J., Molemaker, M.J., McWilliams, J.C., 2014. Submesoscale cold filaments in the gulf stream. J. Phys. Oceanogr. 44, 2617–2643.
Gula, J., Molemaker, M.J., McWilliams, J.C., 2016. Submesoscale dynamics of a gulf stream frontal eddy in the South Atlantic bight. J. Phys. Oceanogr. 46, 305–325.
Haney, R.L., 1991. On the pressure gradient force over steep topography in sigma coordinate ocean models. J. Phys. Oceanogr. 21, 610–619.
Hetland, R.D., 2017. Suppression of baroclinic instabilities in buoyancy-driven flow over sloping bathymetry. J. Phys. Oceanogr. 47, 49–68.
Jakob, D., Su, C., Eizenberg, N., Kociuba, G., Steinle, P., Fox-Hughes, P., Bettio, L., 2017. An atmospheric high-resolution regional reanalysis for Australia. BAMOS 30 (3), 16–23 (September).
Kerry, C.G., Powell, B.S., Roughan, M., Oke, P.R., 2016. Development and evaluation of a high-resolution reanalysis of the East Australian Current region using the Regional Ocean Modelling System (ROMS 3.4) and Incremental Strong-Constraint 4-Dimensional Variational (IS4D-Var) data assimilation. Geosci. Model Dev. 9, 3779–3801. https://doi.org/10.5194/gmd-9-3779-2016.
Kerry, C.G., Roughan, M., Powell, B.S., 2018. Observation impact in a regional reanalysis of the east Australian current system. J. Geophys. Res. Oceans 123.
Lévy, M., Klein, P., Treguier, A., 2001. Impacts of sub-mesoscale physics on production and subduction of phytoplankton in an oligotrophic regime. J. Mar. Res. 59 (535-565).
Lévy, M., Klein, P., Tréguier, A., Iovino, D., Madec, G., Masson, S., Takahashi, K., 2010. Modifications of gyre circulation by sub-mesoscale physics. Ocean Model. 34, 1–15 (April).
Lindzen, R.S., Farrell, B., 1980. A simple approximate result for the maximum growth rate of baroclinic instabilities. J. Atmos. Sci. 37, 1648–1654.
Luo, H., Bracco, A., Cardona, Y., McWilliams, J.C., 2016. Submesoscale circulation in the northern Gulf of Mexico: surface processes and the impact of the freshwater river input. Ocean Model. 101, 68–82 (March).
Mantovanelli, A., Keating, S., Wyatt, L.R., Roughan, M., Schaeffer, A., 2017. Lagrangian and Eulerian characterization of two counter-rotating submesoscale eddies in a western boundary current. J. Geophys. Res. Oceans 122, 4902–4921.
Mellor, G.L., Ezer, T., Oey, L.Y., 1994. The pressure gradient error conundrum of sigma coordinate ocean models. J. Atmos. Ocean. Technol. 11, 1126–1134.
Metzger, E., Smedstad, O., Thoppil, P., Hurlburt, H., Cummings, J., Wallcraft, A., Zamudio, L., Franklin, D., Posey, P., Phelps, M., Hogan, P., Bub, F., DeHaan, C., 2014. US Navy operational global ocean and Arctic ice prediction systems. Oceanography 27 (3), 32–43.
Moore, A.M., Arango, H.G., Broquet, G., Powell, B.S., Zavala-Garay, J., Weaver, A.T., 2011. The Regional Ocean Modeling System (ROMS) 4-dimensional variational data assimilation systems: Part I - System overview and formulation. Prog. Oceanog. 91, 34–49.
Oke, P., Sakov, P., Cahill, M.L., Dunn, J.R., Fiedler, R., Griffin, D.A., Mansbridge, J.V., Ridgway, K.R., Schiller, A., 2013. Towards a dynamically balanced eddy-resolving ocean reanalysis: BRAN3. Ocean Model. 67, 52–70.
Oke, P.R., Brassington, G.B., Griffin, D.A., Schiller, A., 2008. The Bluelink ocean data assimilation system (BODAS). Ocean Model. 21, 46–70.
Oke, P.R., Middleton, J.H., 2000. Topographically induced upwelling off eastern Australia. J. Phys. Oceanogr. 30, 512–530.
Oke, P.R., Roughan, M., Cetina-Heredia, P., Pilo, G.S., Ridgway, K.R., Rykova, T., Archer, M.R., Coleman, R.C., Kerry, C.G., Rocha, C., Schaeffer, A., Vitarelli, E., 2019. Revisiting the circulation of the East Australian current: its path, separation, and eddy field. Prog. Oceanogr.
Puri, K., Dietachmayer, G., Steinle, P., Dix, M., Rikus, L., Logan, L., Naughton, M., Tingwell, C., Xiao, Y., Barras, V., Bermous, I., Bowen, R., Deschamps, L., Franklin, C., Fraser, J., Glowacki, T., Harris, B., Lee, J., Le, T., Roff, G., Sulaiman, A., Sims, H., Sun, X., Sun, Z., Zhu, H., Chattopadhyay, M., Engel, C., 2013. Operational implementation of the ACCESS Numerical Weather Prediction system. Aust. Meteorol. Oceanogr. J. 63, 265–284 (January).
Qiu, B., Chen, S., Klein, P., Sasaki, H., Sasai, Y., 2014. Seasonal mesoscale and submesoscale eddy variability along the north pacific subtropical countercurrent. J. Phys. Oceanogr. 44, 3079–3098 (December).
Roughan, M., Keating, S., Schaeffer, A., Heredia, P.C., Rocha, C., Griffin, D., Robertson, R., Suthers, I., 2017. A tale of two eddies: the bio-physical characteristics of two contrasting cyclonic eddies in the East Australian Current. J. Geophys. Res. Oceans 122.
Roughan, M., Kerry, C., McComb, P., 2018. New Frontiers in Operational Oceanography. GODAE OceanView. In: Ch. 4: Shelf and Coastal Ocean Observing and Modeling Systems: A New Frontier in Operational Oceanography, pp. 91–116 (September).
Roughan, M., Middleton, J.H., 2004. On the East Australian Current: variability, encroachment and upwelling. J. Geophys. Res. 109 (C07003).
Roughan, M., Morris, B.D., Suthers, I.M., 2010. NSW-IMOS: an integrated marine observing system for southeastern Australia. IOP Conf. Ser. Earth Environ. Sci. 11 (012030).
Roughan, M., Schaeffer, A., Suthers, I.M., 2015. Coastal ocean observing systems. In: Ch. 6: Sustained Ocean Observing along the Coast of Southeastern Australia: NSW-IMOS 2007-2014. Academic Press, pp. 76–98 (December).
Sandery, P.A., Sakov, P., 2017. Ocean forecasting of mesoscale features can deteriorate by increasing model resolution towards the submesoscale. Nat. Commun. 8 (1566).
Schaeffer, A., Gramoulle, A., Roughan, M., Mantovanelli, A., 2017. Characterizing frontal eddies along the East Australian Current from HF radar observations. J. Geophys. Res. Oceans 122 (5), 3964–3980 (May).
Sloyan, B.M., Ridgway, K.R., Cowley, R., 2016. The east australian current and property transport at 27S from 2012-2013. J. Phys. Oceanogr. 46 (3) (March).
Stewart, K.D., Hogg, A.M., Griffies, S.M., Heerdegen, A.P., Ward, M.L., Spence, P., England, M.H., 2017. Vertical resolution of baroclinic modes in global ocean models. Ocean Model. 113, 50–65 (May).

Thomas, L.N., Tandon, A., Mahadevan, A., 2008. Submesoscale processes and dynamics. In: Ocean Modeling in an Eddying Regime (AGU Monograph).
Vallis, G.K., 2006. Atmospheric and Oceanic Fluid Dynamics: Fundamentals and Large-Scale Circulation. Cambridge Univ. Press, United Kingdom.
Whiteway, T., 2009. Australian Bathymetry and Topography Grid Scale 1:5000000. Geoscience, Australia, Canberra (June).
Wilkin, J.L., Zhang, W.G., 2007. Modes of mesoscale sea surface height and temperature variability in the East Australian Current. J. Geophys. Res. 112 (C01013).
Wyatt, L.R., 2015. Coastal ocean observing systems. In: Ch. 9: The IMOS Ocean Radar Facility, ACORN. Academic Press, pp. 143–158 (December).
Wyatt, L.R., Mantovanelli, A., Heron, M.L., Roughan, M., Steinberg, C.R., 2018. Assessment of surface currents measured with high-frequency phased-array radars in two regions of complex circulation. IEEE J. Ocean. Eng. 43 (2), 484–505 (April).
Zavala-Garay, J., Wilkin, J.L., Arango, H.G., 2012. Predictability of mesoscale variability in the East Australian Current given strong-constraint data assimilation. J. Phys. Oceanogr. 42, 1402–1420.
Zhong, Y., Bracco, A., 2013. Submesoscale impacts on horizontal and vertical transport in the Gulf of Mexico. J. Geophys. Res. Oceans 118, 5651–5668.
Zou, I.M., Navon, M., Le Dimet, F.X., 1992. An optimal nudging data assimilation scheme using parameter estimation. Q. J. R. Meteorol. Soc. 118 (1), 163–186.